

## A benchmark study of 1-D numerical schemes for arterial blood flow modelling

Etienne Boileau<sup>1</sup>, Perumal Nithiarasu<sup>1\*†</sup>, Pablo J. Blanco<sup>3,4\*†</sup>, Lucas O. Müller<sup>3,4</sup>,  
Fredrik Eikeland Fossan<sup>5</sup>, Leif Rune Hellevik<sup>5\*†</sup>, Wouter P. Donders<sup>6</sup>, Wouter  
Huberts<sup>6\*†</sup>, Marie Willemet<sup>2</sup>, Jordi Alastruey<sup>2\*†</sup>

<sup>1</sup>Zienkiewicz Centre for Computational Engineering, College of Engineering, Swansea University,  
Swansea, SA2 8PP, UK

<sup>2</sup>Division of Imaging Sciences and Biomedical Engineering, St. Thomas' Hospital, King's College London,  
London, SE1 7EH, UK

<sup>3</sup>National Laboratory for Scientific Computing, LNCC/MCTI, Av. Getúlio Vargas 333, 25651-075,  
Petrópolis, RJ, Brazil

<sup>4</sup>National Institute of Science and Technology in Medicine Assisted by Scientific Computing, INCT-MACC,  
Petrópolis, RJ, Brazil

<sup>5</sup>Division of Biomechanics, Norwegian University of Science and Technology, Trondheim, Norway

<sup>6</sup>Faculty of Health, Medicine and Life Sciences, Biomedical Engineering, Maastricht University Medical Centre,  
Maastricht, The Netherlands

### SUMMARY

Hæmodynamical simulations using 1-D computational models exhibit many of the features of the systemic circulation under normal and diseased conditions. Recent interest in verifying 1-D numerical schemes has led to the development of alternative experimental setups and the use of 3-D numerical models to acquire data not easily measured *in vivo*. In most studies to date, only one particular 1-D scheme is tested. In this paper we present a systematic comparison of six commonly used numerical schemes for 1-D blood flow modelling: discontinuous Galerkin (DCG), locally conservative Galerkin (LCG), Galerkin least-squares finite element method (FEM), finite volume method (FVM), finite difference MacCormack (McC), and a simplified trapezium rule method (STM). Comparisons are made in a series of six benchmark test cases with an increasing degree of complexity. The accuracy of the numerical schemes is assessed by comparison against theoretical results, 3-D numerical data in compatible domains with distensible walls, or experimental data in a network of silicone tubes. Results show a good agreement among all numerical schemes and their ability to capture the main features of pressure, flow and area waveforms in large arteries. *All the information used in this study, including the input data for all benchmark cases, experimental data where available, and numerical solutions for each scheme, is made publicly available online, providing a comprehensive reference data set to support the development of 1-D models and numerical schemes.* Copyright © 2012 John Wiley & Sons, Ltd.

Received ...

**KEY WORDS:** 1-D arterial hæmodynamics; 1-D numerical schemes; benchmark test cases; pulse wave propagation

\*Correspondence to: Perumal Nithiarasu, Zienkiewicz Centre for Computational Engineering, College of Engineering, Swansea University, Swansea, SA2 8PP, UK; Jordi Alastruey, Division of Imaging Sciences and Biomedical Engineering, St. Thomas' Hospital, King's College London, London, SE1 7EH, UK; Pablo J. Blanco, National Laboratory for Scientific Computing, LNCC/MCTI, Av. Getúlio Vargas 333, 25651-075, Petrópolis, RJ, Brazil; Leif Rune Hellevik, Department of Structural Engineering, Division of Biomechanics, Norwegian University of Science and Technology, 7491 Trondheim, Norway; Wouter Huberts, Faculty of Health, Medicine and Life Sciences, Biomedical Engineering, PO Box 616, 6200 MD Maastricht, The Netherlands

†E-mail: p.nithiarasu@swansea.ac.uk; jordi.alastruey-arimon@kcl.ac.uk; pjblanco@lncc.br; leif.r.hellevik@ntnu.no; wouter.huberts@maastrichtuniversity.nl

## 1. INTRODUCTION

One-dimensional (1-D) models of blood flow have been extensively used to study wave propagation phenomena in arteries. More recently, this has been extended to the venous circulation. These models allow us to investigate physical mechanisms underlying changes in pressure and flow pulse waveforms that are produced by cardiovascular disease. The 1-D equations thus form the basis of wave analysis tools for extracting clinically relevant information from waveform measurements; *e.g.* separation of waves into forward- and backward-travelling components [1] and wave intensity analysis [2, 3], that may be used for the assessment of cardiovascular function.

In contrast to 3-D fluid-structure interaction models, 1-D models are notably recognised to be computationally inexpensive, thus making them very attractive in applications such as vascular intervention planning, or for serving as boundary conditions for higher dimensional models. Key contributions to 1-D modelling include the studies of Hughes and Lubliner [4], Avolio [5], Stettler *et al.* [6], Stergiopoulos *et al.* [7, 8], Olufsen *et al.* [9], Formaggia *et al.* [10], Sherwin *et al.* [11], Bessems *et al.* [12], Hellevik *et al.* [13, 14, 15], Mynard and Nithiarasu [16], Low *et al.* [17], and more recently Müller and Toro [18, 19], and Blanco *et al.* [20, 21, 22]. For recent reviews on arterial pulse wave haemodynamics see [23, 24]. For a historical overview of this field of research see [25] and the introductions in [4, 11, 23].

An increasing number of recent studies have shown the ability of the 1-D formulation to capture the main features of pressure, flow and area waveforms in large human arteries, using *in vivo* measurements [6, 8, 9, 26, 27], *in vitro* experiments [28, 29, 30, 31, 32], or 3-D numerical data [16, 33]. In [16], both 1-D waveforms and 3-D patient-specific results were presented for a single artery. Recently, an exhaustive comparison between 1-D and 3-D formulations has been published [33], but to date there have been very few comparisons among commonly used numerical schemes for 1-D blood flow modelling.

Different formulations and several corresponding numerical methods have been proposed to solve the 1-D equations, especially in the time domain. These include the method of characteristics [34, 35], finite element methods such as Galerkin [11, 12, 16, 26, 27, 30, 36] and Taylor-Galerkin (combined with operator splitting techniques) [10] schemes, finite volume methods [37, 38, 39], and finite difference methods such as the Lax-Wendroff method [9, 40, 41] and the MacCormack method [13, 31]. Taylor-Galerkin and discontinuous Galerkin 1-D schemes were compared in an idealised artery with abrupt changes in material properties [42], and in a model of the aorta and cerebral arteries [43]. In these studies, however, there was no ‘benchmark’ data to compare with, and in the latter, the emphasis was more on the development of a methodology for parameter estimation than on providing a systematic comparison between numerical schemes. Using a different formulation, Müller and Toro [38] proposed and validated a novel ‘well-balanced’ scheme against the experimental results obtained in [30], but did not provide a cross-comparison among other schemes. Wang *et al.* [44] recently presented a comparison of four numerical schemes (local discontinuous Galerkin, MacCormack, Taylor-Galerkin, and a monotonic upwind scheme for conservation laws), tested on a single tube, a simple bifurcation and a network with 55 arteries. However, they did not rely on experimental or 3-D data to assess the accuracy of their 1-D numerical solutions.

The aim of this paper is to present a comprehensive assessment of six commonly used numerical schemes for arterial 1-D modelling in a series of benchmark test cases. The schemes under consideration are: discontinuous Galerkin (DCG), locally conservative Galerkin (LCG), Galerkin least-squares finite element method (FEM), finite volume method (FVM), finite difference MacCormack (McC), and a simplified scheme that spatially integrates the mass and momentum equations along the vessel axis using the trapezium rule method (STM). The test cases are: (i) a model of blood flow in a reflection-free tube for which a theoretical solution exists; (ii) blood flow in the human common carotid artery, (iii) the upper thoracic aorta, and (iv) the aortic bifurcation, for which 3-D solutions are available from [33] using the numerical scheme described in [45]; (v) blood flow in a network with 37 arterial segments representing the aorta and its largest branches, for which *in vitro* pressure and flow waveforms were acquired in [46]; and (vi) blood flow in the

ADAN56 model, which contains the largest 56 systemic arteries of the human circulation under normal physiological conditions [22]. All data sets presented in this study are made available as supplementary material, in order to facilitate the development and assessment of further numerical schemes.

The outline of this paper is as follows. In Section 2 we describe the 1-D formulation and in Section 3 we present the numerical schemes used in this work, paying special attention to common and particular aspects of each scheme, including the implementation of boundary conditions. In Section 4 we compare the numerical predictions of all six numerical schemes in all six benchmark test cases. Lastly, we discuss the outcome of this comparison in Section 5 and the relevance of the selected test cases for benchmarking 1-D modelling.

## 2. MATHEMATICAL MODEL

### 2.1. One-dimensional formulation

In the 1-D formulation, the computational domain is decomposed into segments connected to each other at nodes. Each segment is modelled as a deformable tube, representing a blood vessel, whose properties are described by a single axial coordinate  $x$ . By assuming the vessel wall to be impermeable and blood to be an incompressible Newtonian fluid, conservation of mass and momentum applied to a control volume of the vessel yields

$$\begin{cases} \frac{\partial A}{\partial t} + \frac{\partial (AU)}{\partial x} = 0 \\ \frac{\partial U}{\partial t} + U \frac{\partial U}{\partial x} + \frac{1}{\rho} \frac{\partial P}{\partial x} = \frac{f}{\rho A} \end{cases}, \quad (1)$$

where  $t$  is the time,  $A(x, t)$  is the cross-sectional area of the tube, or the vessel luminal area,  $P(x, t)$  and  $U(x, t)$  are the cross-sectional average of the pressure and axial velocity, respectively, over the cross-section  $A$ , and  $\rho$  is the constant density of blood. The term  $f(x, t)$  accounts for the frictional force per unit length, and depends on the chosen velocity profile, which is used to estimate the wall shear stress and the convective inertia terms (see [4, 11, 47, 48, 49] and references therein for a complete derivation, including these terms). In this work, the axial velocity profile  $u(x, \xi, t)$  is assumed to be axisymmetric and is given by [48]

$$u(x, \xi, t) = U(x, t) \frac{\zeta + 2}{\zeta} \left[ 1 - \left( \frac{\xi}{r} \right)^\zeta \right], \quad (2)$$

where  $r(x, t)$  is the lumen radius,  $\xi$  is the radial coordinate, and  $\zeta$  is a given constant for a particular profile. Integration of the 3-D Navier-Stokes, and using Eq. (2) yields  $f = -2(\zeta + 2)\mu\pi U$ , with  $\mu$  the dynamic viscosity of blood, here assumed to be constant.

For continuous solutions, there are alternative and equivalent formulations to Eq. (1) (or  $AU$  formulation), written in terms of the area  $A$  and the flow rate  $Q = AU$  ( $AQ$  formulation) [11], or in terms of the pressure and the flow rate ( $PQ$  formulation) [23].

A relationship between  $P$  and  $A$  (or *tube law*) is required to close Eq. (1) and account for the fluid-structure interaction of the problem. Here we consider a relationship of the form [10]

$$P - P_{\text{ext}} = P_d + \frac{\beta}{A_d} \left( \sqrt{A} - \sqrt{A_d} \right), \quad \beta(x) = \frac{4}{3} \sqrt{\pi} E h, \quad (3)$$

where  $P_{\text{ext}}(x)$  is the external pressure,  $P - P_{\text{ext}}$  is the transmural pressure, and  $P_d(x)$ ,  $A_d(x)$  are the diastolic pressure and area, respectively. The term  $\beta(x)$  accounts for the material properties of the arterial wall, modelled here as a thin, incompressible, homogeneous, isotropic, elastic membrane with elastic modulus  $E(x)$  and thickness  $h(x)$ . This type of tube law has been extensively used; e.g. in [5, 9, 10, 11, 13, 16, 26, 27, 33, 40, 41, 42, 46, 48, 49, 50, 51, 52].

## 2.2. Characteristics analysis

Equations (1) and (3) form a system of hyperbolic partial differential equations. A characteristic analysis reveals that for any point in the  $(x, t)$  space, there are two characteristic paths,  $C_f$  and  $C_b$ , defined by

$$C_{f,b} \equiv \frac{d\hat{x}_{f,b}}{dt} = U \pm c, \quad c = \sqrt{\frac{A}{\rho} \frac{\partial P}{\partial A}}, \quad (4)$$

along which the forward ( $W_f$ ) and backward ( $W_b$ ) *characteristic variables* travel.

Under physiological arterial flow conditions, the pulse wave velocity  $c$  is much greater than the maximum convective (average) velocity  $U$ , so that  $U + c > 0$  and  $U - c < 0$  (*i.e.* the flow is subcritical). As a result,  $W_f$  propagates in the forward direction (we define the forward direction as the direction of mean blood flow, in which  $x$  increases) with a speed of  $U + c$  and  $W_b$  propagates in the backward direction with a speed of  $U - c$ . Using Eq. (3) leads to the following expression for the pulse wave velocity

$$c = \sqrt{\frac{\beta}{2\rho A_d}} A^{1/4}. \quad (5)$$

For a detailed analysis, the reader is referred to [11, 13, 14, 24, 47, 53] and references therein.

## 2.3. Boundary conditions

Given that we have a convection-dominated problem with subcritical flow, we need to prescribe one boundary condition at both the inlet and outlet of each arterial domain  $\Omega$ . We classify them into *inflow* (Section 2.3.1), *junction* (Section 2.3.2) and *terminal* (Section 2.3.3) boundary conditions. Their implementation is briefly described in Section 3.7.

**2.3.1. Inflow boundary condition** In all test cases presented below, the total volume flow rate  $Q_{in}(t)$  is imposed at the inlet of single-domain models (Sections 4.1, 4.2 and 4.3) or at the root of network models (Sections 4.4, 4.5 and 4.6), *i.e.*

$$Q = Q_{in}(t), \quad (6)$$

where  $Q_{in}(t)$  is a given function of time.

**2.3.2. Junction matching conditions** In the 1-D formulation, coupling conditions have to be enforced between arterial domains  $\Omega$  and at junctions, where nodes connecting each segment are treated as discontinuities. At a junction with  $N$  converging vessels, the coupling equations are the conservation of mass and the continuity of total pressure, *i.e.*

$$\sum_{i=1}^N A_i U_i = 0, \quad (7)$$

$$P_1 + \frac{\rho}{2} U_1^2 = P_i + \frac{\rho}{2} U_i^2 \quad i = 2, \dots, N. \quad (8)$$

In most schemes, compatibility conditions on the propagating characteristic variables also need to be enforced, see Section 3.7.2.

**2.3.3. Terminal boundary conditions** In peripheral vessels (small arteries, arterioles and capillaries), fluid resistance dominates over wall compliance and fluid inertia. The effect of peripheral resistance on pulse wave propagation in large 1-D model arteries is commonly simulated using linear lumped parameter models (or zero-dimensional (0-D) models) coupled to 1-D model terminal branches. In this study, we use the following three types of terminal boundary conditions: completely absorbent outflow conditions, single-resistance models, or matched three-element Windkessel models. The latter is required in models in which peripheral vessels include large compliant arteries. This model relates the pressure and the flow at the end point of a terminal domain

$\Omega$  through

$$Q \left( 1 + \frac{R_1}{R_2} \right) + CR_1 \frac{\partial Q}{\partial t} = \frac{P - P_{\text{out}}}{R_2} + C \frac{\partial P}{\partial t}. \quad (9)$$

It consists of a resistance  $R_1$  connected in series with a parallel combination of a second resistance  $R_2$  and a compliance  $C$  (Fig. 1). The resistance  $R_1$  is equal to the characteristic impedance of the end point in  $\Omega$  to minimise wave reflections [50].

More sophisticated terminal models include 0-D models with time-dependent resistances to simulate flow control mechanisms [50], single tapering vessels [16, 17], structured-tree networks and impedance boundary conditions [9, 54, 55], to capture wave propagation phenomena in downstream vessels, and 0-D compartmental models of parts of the cardiovascular system that are not simulated using the 1-D formulation (*e.g.* the chambers of the heart, the venous valves and circulation, etc.) [18, 19, 41, 56, 57, 58].

### 3. NUMERICAL METHODS

This section outlines the six numerical schemes used in this work. We focus on highlighting common and particular aspects of each method and refer the reader to our previous papers in which these schemes are described in detail. Each segment of the computational domain  $\Omega$  is discretised according to the chosen method, using either finite elements (DCG, LCG, FEM), finite volumes (FVM), finite differences (McC), or any equivalent spatial discretisation (STM). In order to define the characteristic spatial discretisation, an element, a cell or finite difference stencil are equally referred to as  $\Omega_e$ .

#### 3.1. Discontinuous Galerkin (DCG) scheme

The DCG scheme solves Eq. (1) written in conservative form together with the tube law given by Eq. (3). The discrete weak form is obtained by multiplying the resulting system by Galerkin test functions, which belong to the finite space of piecewise polynomial vector functions, and by integrating over the domain  $\Omega$ . The solution vector is expanded using high-order Legendre polynomials, which may be discontinuous across inter-element boundaries, resulting in a spectral/*hp* spatial discretisation. Information is propagated between elemental regions  $\Omega_e$  through a flux term, using the characteristics variables introduced in Section 2.2. Time integration is performed by means of an explicit second-order Adams-Bashforth method. The Courant-Friedrichs-Lewy (CFL) limit that imposes a restriction on the maximum time step is fixed by the time-integration scheme and discretisation [59]. A detailed description of this scheme is given in [24], and a description of the spectral/*hp* element method in [60].

#### 3.2. Locally conservative Galerkin (LCG) scheme

The LCG method is based on a standard finite element Galerkin procedure, with the addition of Taylor-Galerkin stabilisation [42]. The scheme is derived as in the DCG method, but the solution vector is expanded using a piecewise linear approximation. Elements  $\Omega_e$  are treated as sub-domains with their own boundaries, so that only small systems are solved locally and independently of one another, *i.e.* without the need for assembling global arrays. Information is propagated between elements at each time step using interface fluxes. At global mesh nodes, contributions from different elements are averaged to provide a unique solution. The resulting equations must satisfy the CFL stability condition. See [16, 17, 61] for a detailed exposition and further references.

#### 3.3. Galerkin Least-Squares Finite Element Method (FEM)

In the FEM, the equivalent  $AQ$  formulation is rewritten in characteristic form and discretised in time using an implicit finite difference Euler scheme. A least-squares approach is used to formulate a variational problem on top of which a Galerkin finite element method is employed for the spatial discretisation. The method is implicit, requiring the assembly of the matrix system at each time

step. However, no CFL constraint must be satisfied. First-order spatial approximation is used and nonlinearities are treated using fixed point iterations. See [36] for a detailed exposition.

### 3.4. Finite Volume Method (FVM)

System of Eqs. (1)-(3) is written in terms of conserved variables  $AQ$  and reformulated as proposed in [37] in order to treat varying mechanical properties up to the limiting case of discontinuous properties. The resulting non-conservative system is solved using a finite-volume type numerical scheme [62]. The numerical scheme is fully explicit and allows for arbitrary space-time accuracy. In order to preserve the space-time accuracy at bifurcations, a special treatment is applied [39]. The time step is computed adaptively at each time iteration, in order to satisfy the corresponding CFL condition.

### 3.5. MacCormack (McC) scheme

The McC scheme solves Eqs. (1)-(3) written in their equivalent  $PQ$  formulation. The equations are discretized with an explicit MacCormack scheme, which is second order in time and space [63]. Due to the explicit formulation, the solutions in each elemental region  $\Omega_e$  may be solved independently (*i.e.* in parallel), but stability requires a CFL condition to be fulfilled. Similar to the DCG scheme above, characteristic variables (Riemann invariants) are used to provide boundary conditions between elemental regions  $\Omega_e$ . A detailed description of the McC scheme is given in [14] and examples of how it is embedded in an uncertainty quantification framework are given in [15].

### 3.6. Simplified Trapezium Rule Method (STM)

The STM scheme solves the  $PQ$  system for a domain discretised into non-overlapping two noded elements after linearisation, time discretisation and spatial integration along the vessel axis. Linearisation is performed by Newton's method up to first order, time discretization is achieved using a second order backward difference scheme and integration is done using the trapezium rule. It can be shown that continuity of static pressure is automatically satisfied using this method, and thus no additional coupling equations are required. For more details regarding the numerical scheme, we refer the reader to [64].

### 3.7. Implementation of boundary conditions

**3.7.1. Inflow boundary condition** To avoid spurious reflections in the DCG, FVM, LCG and McC schemes, values of the primitive variables are determined from the prescribed flow rate using the characteristic variables, following the same procedure as described below for terminal boundary conditions. For the FEM, the inflow condition is strongly imposed in the system matrix by replacing the incoming characteristic equation by the boundary condition. For the STM method, however, enforcing continuity of propagating characteristic variables is not required.

**3.7.2. Junction matching conditions** For the DCG, FVM, LCG and McC schemes, arterial domains are connected at junctions by enforcing Eqs. (7)-(8) and compatibility conditions on the propagating characteristic variables. For the FEM, these conditions are directly imposed in the matrix of the system by replacing the outgoing characteristic equation in each vessel with the corresponding coupling condition. For the STM method, conservation of mass is automatically satisfied during assembly of the large matrices, and it is not required to enforce continuity of the characteristic variables. In this scheme, the dynamic part of pressure ( $1/2\rho U^2$ ) is neglected at junctions.

**3.7.3. Terminal boundary conditions** Numerically, Eq. (9) is implemented through the solution of a Riemann problem at the 1-D/0-D interface for the DCG [24], LCG, FVM [18], and McC [14] formulations. As with junction matching conditions above, in the FEM scheme, this terminal condition, discretised in time with an implicit Euler method, is imposed in the matrix of the system by replacing the outgoing characteristic equation of the terminal branch [36]. The STM method has pressure as the only state variable, which enables an extension of the 1-D pulse wave



propagation model with 0-D models describing peripheral haemodynamics without the need of additional coupling equations [64].

### 3.8. Error calculations

For the test cases presented in Sections 4.2 to 4.4, the numerical solutions of pressure ( $P$ ), pressure difference between inlet and outlet ( $\Delta P$ ), volumetric flow rate ( $Q$ ), and change in radius from diastole ( $\Delta r$ ) given by the six 1-D formulations are compared with corresponding values provided by the 3-D formulation in Xiao *et al.* [33]. For the 37-artery network (Section 4.5),  $P$  and  $Q$  are compared in selected arterial sites with corresponding *in vitro* data measured by Matthys *et al.* [46]. We use the following relative error metrics for  $P$  and  $Q$ :

$$\mathcal{E}_P^{RMS} = \sqrt{\frac{1}{n} \sum_{i=1}^n \left( \frac{P_i^{1D} - \mathcal{P}_i}{\mathcal{P}_i} \right)^2}, \quad \mathcal{E}_Q^{RMS} = \sqrt{\frac{1}{n} \sum_{i=1}^n \left( \frac{Q_i^{1D} - \mathcal{Q}_i}{\max_j(\mathcal{Q}_j)} \right)^2}, \quad (10)$$

$$\mathcal{E}_P^{MAX} = \max_i \left| \frac{P_i^{1D} - \mathcal{P}_i}{\mathcal{P}_i} \right|, \quad \mathcal{E}_Q^{MAX} = \max_i \left| \frac{Q_i^{1D} - \mathcal{Q}_i}{\max_j(\mathcal{Q}_j)} \right|, \quad (11)$$

$$\mathcal{E}_P^{SYS} = \frac{\max(P^{1D}) - \max(\mathcal{P})}{\max(\mathcal{P})}, \quad \mathcal{E}_Q^{SYS} = \frac{\max(Q^{1D}) - \max(\mathcal{Q})}{\max(\mathcal{Q})}, \quad (12)$$

$$\mathcal{E}_P^{DIAS} = \frac{\min(P^{1D}) - \min(\mathcal{P})}{\min(\mathcal{P})}, \quad \mathcal{E}_Q^{DIAS} = \frac{\min(Q^{1D}) - \min(\mathcal{Q})}{\max(\mathcal{Q})}, \quad (13)$$

where  $P_i^{1D}$  and  $Q_i^{1D}$  are the results obtained from each 1-D solution at a given spatial location and time point  $i$  ( $i = 1, \dots, n$ ). At the same spatial location and time point  $i$ ,  $\mathcal{P}_i$  and  $\mathcal{Q}_i$  are either the cross-sectional averaged pressure and flow from the 3-D model or the instantaneous values measured *in vitro*. The number of time points  $n$  is determined by the 3-D solution or experimental sampling rate (1 kHz).  $\mathcal{E}_P^{RMS}$  and  $\mathcal{E}_Q^{RMS}$  are the root mean square relative errors for pressure and flow;  $\mathcal{E}_P^{MAX}$  and  $\mathcal{E}_Q^{MAX}$  are the maximum relative errors in pressure and flow;  $\mathcal{E}_P^{SYS}$  and  $\mathcal{E}_Q^{SYS}$  are the errors in systolic pressure and flow; and  $\mathcal{E}_P^{DIAS}$  and  $\mathcal{E}_Q^{DIAS}$  are the errors in diastolic pressure and flow, respectively. Flow errors are normalized by the maximal flow over the cardiac cycle to avoid division by small values of flow. For the quantities  $\Delta P$  and  $\Delta r$  we use the same metrics as for the flow rate. All error metrics are calculated over a single cardiac cycle, once the numerical results are in the periodic regime.

## 4. RESULTS

We first compare the solutions given by the six numerical schemes described above in a series of simple test cases: a model of blood flow in a reflection-free tube for which a theoretical solution exists in the limit of negligible fluid velocity (Section 4.1), and models of blood flow in the human common carotid artery (Section 4.2), upper thoracic aorta (Section 4.3) and aortic bifurcation (Section 4.4), for which 3-D solutions are available from [33]. We then assess the six schemes in two different arterial networks: a 37-artery model of the aorta and its largest branches for which *in vitro* pressure and flow waveforms were acquired in [46] (Section 4.5), and the ADAN56 model by Blanco *et al.* [22], which contains the largest 56 systemic arteries of the human circulation (Section 4.6). For each test case, we provide graphical comparisons supported by tabulated calculations of relative errors. Table I shows the time step, characteristic spatial discretisation (characteristic length of  $\Omega_e$ ), the CFL number, space and time accuracies for each scheme.

#### 4.1. Single pulse propagation in a straight reflection-free vessel

This test simulates the propagation of a narrow Gaussian-shaped wave in a single vessel with uniform parameters and a completely absorbent outflow boundary condition; *i.e.* with a zero reflection coefficient that absorbs any incident wave [43]. The theoretical solution considered here is that of a linearised system, which is consistent with Eqs. (1)-(3) for the case of small fluid velocity.

The parameters of this model, which we refer to as the *single-pulse model*, are given in Table II. At the inlet, a volume inflow rate with a peak value of  $1 \text{ ml s}^{-1}$  is prescribed using the function

$$Q_{\text{in}}(t) = 10^{-6} \exp(-10000(t - 0.05)^2) \text{ m}^3 \text{ s}^{-1}, \quad (14)$$

with  $t$  given in seconds. The solution is determined using Eq. (3) with  $A_d = A_0$  and  $P_d = P_{\text{ext}} = 0$ . Two different values of blood viscosity ( $\mu$ ) are considered:  $\mu = 0$  (inviscid problem) and  $\mu = 4 \text{ mPa s}$  (viscous problem).

Figure 2 shows the normalized pressure wave at different times along the length of the tube. The inflow has a width of approximately  $0.05 \text{ s}$  and a wave speed of  $c_0 = 6.17 \text{ m s}^{-1}$  at the initial area  $A_0$ , giving a wavelength of about  $c_0 T \approx 31 \text{ cm}$ . This is a short wavelength compared with the  $10 \text{ m}$  long vessel, which enables showing the full shape of the pulse wave as it propagates along the vessel. For the inviscid problem, theoretical pressure and flow waveforms are in phase, have a constant amplitude, and propagate to the right with a wave speed given by Eq. (5) [43]. These theoretical results are well predicted by all six numerical schemes. In particular, in the inviscid case the peak magnitude of the pressure wave ( $P_{\text{peak,inv}}$ ) decreases by less than  $0.9\%$ , relative to the peak magnitude at the inlet, as it travels the length of the vessel. For the viscous problem, the peak magnitude of the pressure wave ( $P_{\text{peak,visc}}$ ) decreases with distance  $x$  from the inlet, with good agreement between numerical results and the asymptotic exponential damping rate given by the theoretical solution

$$P_{\text{peak,visc}}(x) = P_{\text{peak,inv}} \exp\left(-\frac{(\zeta + 2)\pi\mu x}{\rho c_0 A_0}\right). \quad (15)$$

This theoretical solution is indicated by the thick black line in each panel of Fig. 2.

#### 4.2. Common carotid artery

The common carotid artery is simulated as a single vessel with uniform properties coupled to a three-element lumped parameter model of the rest of the systemic circulation [33]. The initial area  $A_0$  that yields the reference diastolic area  $A_d$  at  $P = P_d$  is calculated using

$$A_0 = A_d \left(1 - \sqrt{A_d \frac{P_d}{\beta}}\right)^2. \quad (16)$$

This expression follows from Eq. (3) by considering  $P = 0$ ,  $A = A_d$  and solving for  $A_0$ . The parameters of this model are given in Table III. The inflow boundary condition  $Q_{\text{in}}(t)$  is an *in vivo* signal taken from [33] and is available in the supplementary material.

Figure 3 shows the pressure, pressure difference (between inlet and outlet pressures), flow, and variations in luminal radius with time at the midpoint of the vessel obtained by solving the 1-D equations using all six schemes. These waveforms are almost identical to the corresponding waveforms calculated by solving the Navier-Stokes equations in a 3-D domain with compatible geometrical and mechanical properties and identical inflow and outflow boundary conditions [33]. Relative errors were determined with respect to the 3-D solution and are presented in Table IV. Pressure and flow errors are smaller than errors in pressure difference and variations in radius, with no significant differences between the six schemes. Relative root mean square errors are smaller than  $1.0\%$  for pressure, flow and change in radius, and smaller than  $5.0\%$  for the pressure difference.

#### 4.3. Upper thoracic aorta

The thoracic aorta from the aortic root to the descending aorta is simulated as a single vessel with uniform properties coupled to a three-element lumped parameter model of the rest of the systemic



circulation [33]. The parameters of this model are displayed in Table V. The initial area  $A_0$  is calculated using Eq. (16). The inflow boundary condition  $Q_{in}(t)$  is an *in vivo* signal taken from [33] and is available in the supplementary material.

Figure 4 presents numerical results for the pressure, pressure difference, flow rate, and variations in luminal radius with time at the midpoint of the segment. They are calculated for all six numerical schemes and compared with the corresponding 3-D solutions. The 1-D solutions are similar to each other, with the largest differences with respect to the 3-D results observed during the systolic part of the cardiac cycle. The smallest relative errors are for the pressure and the largest for the pressure difference (Table VI). Relative root mean square errors are all smaller than 3% for the pressure, flow and change in radius, and smaller than 8% for the pressure difference.

#### 4.4. Aortic bifurcation

Before considering a complete network of arteries, we simulate the abdominal aorta branching into the two iliac arteries using a symmetric, single-bifurcation model [33]. Both iliac arteries are coupled to a three-element lumped parameter model of the rest of the systemic circulation. The parameters of this model are shown in Tab. VII. Initial areas are calculated using Eq. (16). The inflow boundary condition  $Q_{in}(t)$  is an *in vivo* signal taken from [33] and is available in the supplementary material.

Figure 5 displays the waveforms for pressure, flow rate, and variations in luminal radius at three points: the midpoint of the aorta, end point of the aorta and midpoint of either iliac artery. All these waveforms are similar among the six schemes and compare well with the corresponding 3-D model waveforms. Relative errors were determined with respect to the 3-D solution and are shown in Table VIII. Relative errors for the pressure and flow rate are consistently smaller than for the change in radius, with no significant differences between the six schemes. Relative root mean square errors are all smaller than 1.2% for the pressure and flow, and smaller than 4.4% for the variation in radius.

#### 4.5. 37-artery network

We simulate the arterial tree presented in Matthys *et al.* [46], for which *in vitro* pressure and flow measurements were acquired at multiple locations. The tree is made up of 37 silicone vessels representing the largest central systemic arteries of the human vascular system. At the inlet of the ascending aorta, the flow rate measured *in vitro* is prescribed as the inflow boundary condition  $Q_{in}(t)$ , which is specified in the supplementary material. Terminal vessels are coupled to single resistors that are simulated as single-resistance terminal models. The 1-D governing equations are solved using the tube law given by Eq. (3) with  $A_d = A_0$  and  $P_d = 0$ , and the initial conditions  $(A(x, 0), U(x, 0), P(x, 0)) = (A_0(x), 0, 0)$  for all segments. General parameters of this model are given in Table IX. For a complete set of parameters we refer the reader to [30, 46] and to the supplementary material.

Comparisons between experimental and numerical pressure and flow waveforms are shown in Fig. 6 for the aorta, and in Figs. 7, 8 and 9 for vessels of the first, second and third generation of bifurcations, respectively. All six numerical schemes are able to capture the main features of *in vitro* pressure and flow waveforms at the eight arterial sites investigated. However, numerical predictions overestimate the amplitude of the high-frequency oscillations observed in the *in vitro* pressure and flow waveforms of vessels of the second (Fig. 8) and third (Fig. 9) generation of bifurcations. Table X shows relative errors calculated with respect to *in vitro* measurements at the eight arterial vessels studied. Relative errors for the pressure are all consistently smaller than for the flow rate, with no significant differences between the six schemes. Relative root mean square errors are all smaller than 4% for the pressure and smaller than 26% for the flow rate.

#### 4.6. ADAN56 model

The last benchmark model considered to test 1-D numerical schemes is a reduced version of the anatomically-detailed arterial network (ADAN) model developed by Blanco *et al.* [21, 22]. The model contains the largest 56 vessels of the human arterial system, as described in [22], and is

represented by 61 arterial segments. Hereafter, we refer to this model as *ADAN56*. The topology of the network is shown in Fig. 10 and the description of the vessels is given in Tables XII–XIII. The inflow boundary condition  $Q_{\text{in}}(t)$  is inspired from one of the inflow signals reported in [65], and is also given in the supplementary material. The tube law is given by Eq. (3), with constant Young moduli throughout the arterial network,  $A_d = A_0$  and  $P_d = P_0 = 10$  kPa. Wall thickness is calculated using the following empirical expression [22]

$$h = R_0 [\tilde{a} \exp(\tilde{b} R_0) + \tilde{c} \exp(\tilde{d} R_0)], \quad (17)$$

where  $R_0$  is the reference radius (related to  $A_0$ ),  $\tilde{a} = 0.2802$ ,  $\tilde{b} = -5.053 \text{ cm}^{-1}$ ,  $\tilde{c} = 0.1324$  and  $\tilde{d} = -0.1114 \text{ cm}^{-1}$ . The initial conditions are  $(A(x, 0), U(x, 0), P(x, 0)) = (A_0(x), 0, P_0)$  for all segments.

Comparisons of pressure and flow rate waveforms obtained using the different numerical techniques are shown in Fig. 11 for three aortic segments, and in Figs. 12, 13 and 14 for first-, second-, third- and fourth-generation vessels, respectively. We observe here that the brachiocephalic branching is not considered as a generation, and that the upper body vessels in the right side keep the same generation as the left vessels. There is an excellent agreement among all waveforms generated by the DCG, LCG, FEM, FVM and McC methods; differences cannot be appreciated in the scale of the figures. Some discrepancies, however, can be observed between these waveforms and those provided by the STM scheme. In addition, Fig. 15 presents a comparison of the pressure variation throughout the aorta at several time instants during the cardiac cycle. These results also illustrate how changes in material properties and branching affect the pressure flow waveforms throughout the cardiac period. In the *ADAN56* model, the first major branches of the aorta are situated at about 30 cm downstream of the aortic root, affecting the pressure waves as observed in Fig. 15. Lastly, Fig. 16 shows that all six schemes produce similar diastolic pressures along the aorta. Some discrepancies are also observed for systolic and mean pressures for the STM scheme, where it overestimates systolic pressures by about 1% in proximal locations and underestimates them by about 3% in distal locations, relative to the values calculated by the other five methods.

## 5. DISCUSSION

We have compared the solution provided by six distinct numerical schemes for nonlinear 1-D blood flow modelling in a set of benchmark test cases. The schemes were chosen to embrace a variety of techniques for the numerical solution of the 1-D formulation: finite element (DCG, FEM, LCG, STM), finite volume (FVM) and finite difference (McC) methods. In this study, we have considered the widely used form of the 1-D equations (1) and (3), which accounts for nonlinear effects and is able to provide physiological features of human pulse waveforms. It is important to note that some of the numerical schemes presented in this study have been used to solve more complex 1-D formulations than the one considered here; *e.g.* Eq. (1) with a visco-elastic tube law [29, 30, 66], or with highly nonlinear terms [12, 15, 18, 21, 22]. However, assessing more complex 1-D formulations is beyond the scope of this study.

Our study has been motivated by the scarceness of test cases for benchmarking 1-D numerical schemes, as well as by our desire to provide an accessible reference dataset. To address this gap in the literature, we have chosen six test cases that collectively provide a comprehensive framework for the development and assessment of other numerical schemes. In large arteries, the wave propagation speed, or pulse wave velocity, is typically larger than the average flow speed. As mentioned previously, under these conditions we do not observe shock formation. The challenge for the numerical schemes tested in these benchmark problems is thus to propagate waves for several periods without excessive errors in amplitude and phase. With this aim in mind, we have fully described all test cases in Sections 4.1 to 4.6 and have provided, as supplementary material, all numerical and *in vitro* data used in this study. The test cases range from a simple, non-physiological, reflection-free single tube, to more physiological single-vessel models, and to network models simulating blood flow in the largest arteries of the human systemic circulation under

normal physiological conditions. In Sections 5.1 to 5.3 we discuss the value of each test case for benchmarking 1-D schemes and examine similarities and discrepancies in the solutions computed by the DCG, LCG, FEM, FVM, McC and STM methods.

### 5.1. Single pulse model

In the linear regime, a theoretical solution exists for the propagation of a narrow Gaussian-shaped wave in a reflection-free vessel, for both inviscid and viscous flow. This wave, which features a small wavelength compared to the vessel length ( $\approx 31$  cm versus 10 m, Fig. 2), is a continuous approximation to the unit pulse  $\delta(t - t_0)$ ,  $t_0 = 0.05$  s (*i.e.*  $\delta(t_0) = 1$  and  $\delta(t) = 0$  for  $t \neq t_0$ ). Thus, very high frequencies dominate the Gaussian-shaped wave considered here. Numerically this is more challenging than the propagation of low-frequency pulse waves. Capturing the correct propagation of high-frequency waves is important for simulating arterial pulse wave haemodynamics under physiological conditions, since higher frequencies are responsible for relevant features of pulse waveforms; *e.g.* the feet of pressure, flow and area waveforms, and the dicrotic notch in the aortic pressure waveform. Our results have shown the ability of all six schemes to solve correctly Eqs. (1) and (3) in the single-pulse model.

### 5.2. Physiological single artery models

We have considered two single-vessel test cases under normal physiological conditions and for which 3-D solutions are available from [33]. These cases have allowed us to show that the six 1-D model schemes are able to capture the main features of 3-D pressure, flow and area waveforms in two large arteries: the common carotid artery (Fig. 3) and the upper thoracic aorta (Fig. 4). For all six schemes, relative errors were consistently smaller for the carotid (Table IV) than the aorta (Table VI) model. This is due to inertial forces playing a larger role in the aorta model; the peak Reynolds number is nearly an order of magnitude greater in the aorta model [33]. As a result, for the aorta model, the nonlinear convective acceleration term in the balance of momentum Eq. (1) has a more significant weight relative to the other terms, making it a more challenging test for 1-D schemes. Larger wall strains ( $\Delta r/r_d$ ) in the aorta model were also identified in [33] as an additional source of discrepancy between 1-D and 3-D modelling. Moreover, relative errors in the aorta model decrease during the diastolic part of the cardiac cycle, since the physics of blood flow becomes increasingly linear and inertia-free with the increasing time in diastole [51].

Compared to the single-pulse test case, pulse wavelengths in the carotid and aorta cases are much longer. These lengths can be approximated by multiplying the period of the systolic part of the inflow wave ( $T_s$ ) with the pulse wave speed at mean pressure ( $c_m$ ); we obtain  $T_s c_m = 2.7$  m for the carotid test and  $T_s c_m = 1.8$  m for the aorta test. As a result, the numerical parameters of all six numerical schemes can be relaxed (see Table I for a comparison).

### 5.3. Physiological network models

The three additional test cases that we have used to assess 1-D numerical schemes contain arterial bifurcations – a key anatomical feature for blood flow modelling in the arterial tree. These are a single-bifurcation model and the 37- and 56-artery models, which contain multiple bifurcations. They allow us to verify the ability of each scheme to deal with multiple reflections generated at a junction, where continuity and compatibility conditions are imposed (Section 2.3.2).

The single-bifurcation model provides a test for benchmarking the connection of three 1-D arterial segments through a bifurcation under normal physiological conditions. This test simulates blood flow in the abdominal aorta and its bifurcation into the two iliac arteries that perfuse the legs. For this test, a 3-D solution is also available from [33]. All six 1-D schemes considered here are able to capture the multiple wave reflections generated at the bifurcation, which shape pressure, flow and area waveforms in the aorta and iliac arteries (Fig. 5). All numerical schemes yield comparable relative errors (Table VIII), despite the dynamic part of the pressure ( $1/2\rho U^2$ ) being neglected in the STM scheme. Moreover, relative root mean square errors are smaller than for the single-aorta

test and similar to the common carotid test, since peak Reynolds numbers are of similar order of magnitude for both the carotid and bifurcation cases.

The 37-artery model includes the aorta and its largest branches. For this case, *in vitro* pressure and flow waveforms were acquired in [46], which has allowed us to test the accuracy of the six 1-D schemes. These are all able to reproduce the main features of pressure and flow waveforms measured *in vitro* (see Figs. 6 to 9), with relative errors smaller than 4% for pressure and 26% for the flow (Table X). Discrepancies between experimental and numerical results arise from the uncertainties in the experimental measurements and the assumptions and simplifications of the 1-D formulation. According to [46], the larger relative errors in the flow predictions compared to their pressure counterparts can be explained because experimental flow measurements were less precise than experimental pressure measurements. High-frequency peripheral oscillations seen in the numerical results may be reduced by adding compliance to the terminal boundary conditions (see Windkessel model Section 2.3.3), but visco-elasticity was shown to have a greater effect on damping the oscillations predicted by the elastic formulation Eq. (3) [30, 46]. Similarly to the single-bifurcation model discussed above, the dynamic part of pressure ( $1/2\rho U^2$ ) was neglected in the STM. Given that the STM produces similar results to the other five methods we conclude that ( $1/2\rho U^2$ ) does not play an important role in the 37-artery model, in accordance with previous observations [46, 67]

In the ADAN56 model, we have simulated blood flow in the 56 largest arteries of the human systemic circulation. Arterial anatomy, mechanical properties, inflow and outflow boundary conditions are all based on physiological human data. Therefore, the ADAN56 model enables verification of numerical methods to solve 1-D haemodynamics under normal physiological conditions. For the ADAN56 model, the six numerical schemes deliver rather consistent solutions. Noticeable discrepancies are obtained with the STM in comparison to the rest of the numerical schemes (see Figs. 11 to 14). Such larger differences are explained by the anatomical configuration of the ADAN56 model, which makes the model more sensitive to the coupling strategy at junctions (in the STM for instance, the dynamic pressure is neglected when coupling vessels at junctions). Differences between models are more visible when zooming in the pressure along the aorta (see Fig. 15). Except for the coupling strategy in the STM discussed above, the rest of the differences can be explained by discretization errors. We note however that such differences between the schemes may be irrelevant for clinical applications, as the observed discrepancies will be negligible with respect to uncertainties from various sources. See for example Eck *et al.* [15], or Chen *et al.* [68] for an uncertainty quantification of simulated pressure waveforms.

## 6. CONCLUSIONS

We have shown that arterial pulse wave haemodynamics can be accurately simulated using finite element, finite volume or finite difference methods. All six schemes considered in this study have been assessed in a series of benchmark test cases with an increasing degree of complexity, for which theoretical, numerical 3-D or *in vitro* pulse waveforms are available. Results have shown a good agreement among all numerical schemes, their ability to solve the nonlinear 1-D equations accurately and to capture the main features of pulse wave propagation in single arterial segments as well as in larger networks. This is consistent with the outcome of previous studies [6, 8, 9, 13, 15, 16, 26, 27, 28, 29, 30, 31, 32, 33]

This study provides additional support for the use of 1-D reduced-order modelling to accurately simulate arterial pulse wave haemodynamics with a reasonable computational cost. The test cases used in this study (and made publicly available as supplementary material) can be applied to facilitate the development and assessment of future numerical schemes for the correct solution of the 1-D equations of blood flow in networks of compliant arteries.

## ACKNOWLEDGEMENT

The authors would like to thank Drs Nan Xiao and Alberto Figueroa for providing all 3-D data used in this study. EB and PN gratefully acknowledge the financial support provided by the Ser Cymru National Research Network in Advanced Engineering and Materials. MW and JA gratefully acknowledge the support of an EPSRC project grant (EP/K031546/1) and the Centre of Excellence in Medical Engineering (funded by the Wellcome Trust and EPSRC under grant number WT 088641/Z/09/Z) and the National Institute for Health Research (NIHR) Biomedical Research Centre at Guys and St Thomas' NHS Foundation Trust in partnership with King's College London. PJB and LOM gratefully acknowledge the support of the Brazilian agencies CNPq and FAPERJ.

## REFERENCES

1. Westerhof N, Sipkema P, Bos GVD, Elzinga G. Forward and backward waves in the arterial system. *Cardiov. Res.* 1972; **6**:648–656.
2. Parker K. An introduction to wave intensity analysis. *Med. Bio. Eng. Comput.* 2009; **47**:175–188.
3. Alastruey J, Hunt A, Weinberg P. Novel wave intensity analysis of arterial pulse wave propagation accounting for peripheral reflections. *Int. J. Numer. Meth. Biomed. Eng.* 2014; **30**:249–279.
4. Hughes T, Lubliner J. On the one-dimensional theory of blood flow in the larger vessels. *Math. Biosciences* 1973; **18**:161–170.
5. Avolio A. Multi-branched model of the human arterial system. *Med. and Biol. Engng. and Comput.* 1980; **18**:709–718.
6. Stettler J, Niederer P, Anliker M. Theoretical analysis of arterial hemodynamics including the influence of bifurcations. Part II: Critical evaluation of theoretical model and comparison with noninvasive measurements of flow patterns in normal and pathological cases. *Ann. Biomed. Eng.* 1981; **9**:165–175.
7. Stergiopulos N, Young D, Rogge T. Computer simulation of arterial flow with applications to arterial and aortic stenoses. *J. Biomech.* 1992; **25**:1477–1488.
8. Reymond P, Bohraus Y, Perren F, Lazeyras F, Stergiopulos N. Validation of a patient-specific one-dimensional model of the systemic arterial tree. *Am. J. Physiol. Heart Circ. Physiol.* 2011; **301**:H1173–H1182.
9. Olufsen M, Peskin C, Kim W, Pedersen E, Nadim A, Larsen J. Numerical simulation and experimental validation of blood flow in arteries with structured-tree outflow conditions. *Ann. Biomed. Eng.* 2000; **28**:1281–1299.
10. Formaggia L, Lamponi D, Quarteroni A. One-dimensional models for blood flow in arteries. *J. Eng. Math.* 2003; **47**:251–276.
11. Sherwin S, Franke V, Peiró J, Parker K. One-dimensional modelling of a vascular network in space-time variables. *J. Eng. Maths.* 2003; **47**:217–250.
12. Bessems D, Rutten M, van de Vosse F. A wave propagation model of blood flow in large vessels using an approximate velocity profile function. *J. Fluid Mech.* 2007; **580**:145–168.
13. Hellevik LR, Vierendeels J, Kiserud T, Stergiopulos N, Irgens F, Dick E. An assessment of ductus venosus tapering and wave transmission from the fetal heart. *Biomech. Model. Mechanobiol.* 2009; **8**(6):509–517.
14. Leinan P. Biomechanical modeling of fetal veins: The umbilical vein and ductus venosus bifurcation. PhD Thesis, Norwegian University of Science and Technology, NTNU, Trondheim, Norway.
15. Eck V, Feinberg J, Langtangen H, Hellevik L. Stochastic sensitivity analysis for timing and amplitude of pressure waves in the arterial system. *Int J Numer Method Biomed Eng* 2015; **31**(4), doi:10.1002/cnm.2711. Epub.
16. Mynard J, Nithiarasu P. A 1D arterial blood flow model incorporating ventricular pressure, aortic valve and regional coronary flow using the locally conservative Galerkin (LCG) method. *Commun. Numer. Meth. Eng.* 2008; **24**:367–417.
17. Low K, van Loon R, Sazonov I, Bevan R, Nithiarasu P. An improved baseline model for a human arterial network to study the impact of aneurysms on pressure-flow waveforms. *Int. J. Numer. Meth. Biomed. Engng.* 2012; **28**:1224–1246.
18. Müller L, Toro E. A global multiscale mathematical model for the human circulation with emphasis on the venous system. *Int. J. Numer. Meth. Biomed. Engng.* 2014; **30**:681–725.
19. Müller L, Toro E. An enhanced closed-loop model for the study of cerebral venous blood flow. *J. Biomech.* 2014; **47**:3361–3372.
20. Blanco P, Watanabe S, Feijóo R. Identification of vascular territory resistances in one-dimensional hemodynamics simulations. *Journal of biomechanics* 2012; **45**(12):2066–2073.
21. Blanco P, Watanabe S, Dari E, Passos M, Feijóo R. Blood flow distribution in an anatomically detailed arterial network model: criteria and algorithms. *Biomech. Model. Mechanobiol.* 2014; **13**:1303–1330.
22. Blanco P, Watanabe S, Passos M, Lemos P, Feijóo R. An anatomically detailed arterial network model for one-dimensional computational hemodynamics. *IEEE Transactions on Biomedical Engineering* 2015; **62**:736–753.
23. van de Vosse F, Stergiopulos N. Pulse wave propagation in the arterial tree. *Annu. Rev. Fluid Mech.* 2011; **43**:467–499.
24. Alastruey J, Parker K, Sherwin S. *Arterial pulse wave haemodynamics*. In Anderson (Ed.) *11th International Conference on Pressure Surges*, chap. 7. Virtual PiE Led t/a BHR Group (ISBN: 978 1 85598 133 1), 2012; 401–442.
25. Parker K. A brief history of arterial wave mechanics. *Med. & Biol. Eng. & Comput.* 2009; **47**:111–118.
26. Steele B, Wan J, Ku J, Hughes T, Taylor C. *In vivo* validation of a one-dimensional finite-element method for predicting blood flow in cardiovascular bypass grafts. *IEEE Trans. Biomed. Eng.* 2003; **50**:649–656.
27. Willemet M, Lacroix V, Marchandise E. Validation of a 1D patient-specific model of the arterial hemodynamics in bypassed lower-limbs: Simulations against *in vivo* measurements. *Med. Eng. Phys.* 2013; **35**:1573–1583.
28. Segers P, Dubois F, Wachter DD, Verdonck P. Role and relevancy of a cardiovascular simulator. *Cardiov. Eng.* 1998; **3**:48–56.
29. Bessems D, Giannopapa C, Rutten M, van de Vosse F. Experimental validation of a time-domain-based wave propagation model of blood flow in viscoelastic vessels. *J. Biomech.* 2008; **41**:284–291.
30. Alastruey J, Khir A, Matthys K, Segers P, Sherwin S, Verdonck P, Parker K, Peiró J. Pulse wave propagation in a model human arterial network: Assessment of 1-D visco-elastic simulations against *in vitro* measurements. *J. Biomech.* 2011; **44**:2250–2258.
31. Saito M, Ikenaga Y, Matsukawa M, Watanabe Y, Asada T, Lagrée PY. One-dimensional model for propagation of a pressure wave in a model of the human arterial network: Comparison of theoretical and experimental results. *J. Biomech. Eng.* 2011; **133**:121 005.
32. Huberts W, Canneyt KV, Segers P, Eloit S, Tordoir J, Verdonck P, van de Vosse F, Bosboom E. Experimental validation of a pulse wave propagation model for predicting hemodynamics after vascular access surgery. *J. Biomech.* 2012; **45**:1684–1691.



33. Xiao N, Alastruey J, Figueroa C. A systematic comparison between 1-D and 3-D hemodynamics in compliant arterial models. *Int. J. Numer. Meth. Biomed. Eng.* 2014; **30**:204–231.
34. Schaaf B, Abbrecht P. Digital computer simulation of human systemic arterial pulse wave transmission: a nonlinear model. *J. Biomech.* 1972; **5**:345–364.
35. Wang J, Parker K. Wave propagation in a model of the arterial circulation. *J. Biomech.* 2004; **37**:457–470.
36. Watanabe S, Blanco P, Feijóo R. Mathematical model of blood flow in an anatomically detailed arterial network of the arm. *ESAIM: Mathematical Modelling and Numerical Analysis* 2013; **47**:961–985.
37. Toro E, Siviglia A. Flow in collapsible tubes with discontinuous mechanical properties: mathematical model and exact solutions. *Communications in Computational Physics* 2013; **13**:361–385.
38. Müller L, Toro E. Well balanced high order solver for blood flow in networks of vessels with variable properties. *Int. J. Numer. Meth. Biomed. Engng.* 2013; **29**:1388–1411.
39. Müller LO, Blanco PJ. A high order approximation of hyperbolic conservation laws in networks: application to one-dimensional blood flow ; Submitted to the Journal of Computational Physics in January 2015.
40. Azer K, Peskin C. A one-dimensional model of blood flow in arteries with friction and convection based on the Womersley velocity profile. *Cardiov. Eng.* 2007; **7**:51–73.
41. Liang F, Takagi S, Himeno R, Liu H. Biomechanical characterization of ventricular–arterial coupling during aging: A multi-scale model study. *J. Biomech.* 2009; **42**:692–704.
42. Sherwin S, Formaggia L, Peiró J, Franke V. Computational modelling of 1D blood flow with variable mechanical properties and its application to the simulation of wave propagation in the human arterial system. *Int. J. Numer. Meth. Fluids* 2003; **43**:673–700.
43. Alastruey J, Passerini T, Formaggia L, Peiró J. Physical determining factors of the arterial pulse waveform: theoretical analysis and estimation using the 1-D formulation. *J. Eng. Math.* 2012; **77**:19–37.
44. Wang X, Fullana J, Lagrée P. Verification and comparison of four numerical schemes for a 1D viscoelastic blood flow model. *Comp. Meths. Biomech. Biomed. Eng.* 2015; **18**:1704.
45. Figueroa C, Vignon-Clemental I, Jansen K, Hughes T, Taylor C. A coupled momentum method for modeling blood flow in three-dimensional deformable arteries. *Comp. Meth. App. Mech. Eng.* 2006; **195**:5685–5706.
46. Matthys K, Alastruey J, Peiró J, Khir A, Segers P, Verdonck P, Parker K, Sherwin S. Pulse wave propagation in a model human arterial network: Assessment of 1-D numerical simulations against *in vitro* measurements. *J. Biomech.* 2007; **40**:3476–3486.
47. Quarteroni A, Formaggia L. *Mathematical modelling and numerical simulation of the cardiovascular system*. In: N. Ayache (ed.), *Modelling of Living Systems*. Elsevier (Amsterdam), 2004.
48. Smith N, Pullan A, Hunter P. An anatomically based model of transient coronary blood flow in the heart. *SIAM J. Appl. Math.* 2002; **62**:990–1018.
49. Čanić S, Kim E. Mathematical analysis of the quasilinear effects in a hyperbolic model of blood flow through compliant axi-symmetric vessels. *Math. Meth. Appl. Sci.* 2003; **26**:1161–1186.
50. Alastruey J, Moore S, Parker K, David T, Peiró J, Sherwin S. Reduced modelling of blood flow in the cerebral circulation: Coupling 1-D, 0-D and cerebral auto-regulation models. *Int. J. Numer. Meth. Fluids* 2008; **56**:1061–1067.
51. Willemet M, Alastruey J. Arterial pressure and flow wave analysis using time-domain 1-D hemodynamics. *Ann. Biomed. Eng.* 2015; **43**:190–206.
52. Coccarelli A, Nithiarasu P. A robust finite element modeling approach to conjugate heat transfer in flexible elastic tubes and tube networks. *Numer. Heat Tr: A-Appl.* 2015; **67**:513–530.
53. Formaggia L, Quarteroni A, Veneziani A (eds.). *Cardiovascular Mathematics. Modeling and simulation of the circulatory system*. Springer-Verlag (Milano), 2009.
54. Brown D. Input impedance and reflection coefficient in fractal-like models of asymmetrically branching compliant tubes. *IEEE Trans. Biomed. Eng.* 1996; **43**:715–722.
55. Cousins W, Gremaud P. Impedance boundary conditions for general transient hemodynamics. *Int. J. Numer. Meth. Biomed. Engng.* 2014; **30**:1294–1313.
56. Quarteroni A, Ragni S, Veneziani A. Coupling between lumped and distributed models for blood flow problems. *Comput. Visual. Sci.* 2001; **4**:111–124.
57. Mynard J, Davidson M, Penny D, Smolich J. A simple, versatile valve model for use in lumped parameter and one-dimensional cardiovascular models. *Int. J. Numer. Meth. Biomed. Engng.* 2012; **28**:626–641.
58. Keijsers J, Leguy S, Parker K, Narracott A, Rittweger J, vande Vosse F. A 1d pulse wave propagation model of the hemodynamics of calf muscle pump function. *Int. J. Numer. Meth. Biomed. Engng.* 2015; .
59. Bolis A, Cantwell C, Kirby R, Sherwin S. From h to p efficiently: optimal implementation strategies for explicit time-dependent problems using the spectral/hp element method. *Int. J. Numer. Meth. Fluids* 2014; **75**:59–607.
60. Karniadakis G, Sherwin S. *Spectral/hp Element Methods for Computational Fluid Dynamics*. Oxford University Press, 2005.
61. Thomas C, Nithiarasu P, Bevan R. The locally conservative Galerkin (LCG) method for solving the incompressible Navier-Stokes equations. *Int. J. Numer. Meth. Fl.* 2008; **57**:1771–1792.
62. Müller LO, Parés C, Toro EF. Well-balanced high-order numerical schemes for one-dimensional blood flow in vessels with varying mechanical properties. *Journal of Computational Physics* 2013; **242**:53–85.
63. Hirsch C. *Numerical Computation of Internal and External Flows, Volume 1: Fundamentals of Numerical Discretization*. Wiley: Brussels, 1989.
64. Kroon W, Huberts W, Bosboom M, van de Vosse F. A Numerical Method of Reduced Complexity for Simulating Vascular Hemodynamics Using Coupled 0D Lumped and 1D Wave Propagation Models. *Computational and Mathematical Methods in Medicine* 2012; **2012**(Article ID: 156094), doi:10.1155/2012/156094.
65. Murgo J, Westerhof N, Giolma J, Altobelli S. Aortic input impedance in normal man: relationship to pressure wave forms. *Circulation* 1980; **62**:105–116.
66. Montecinos GI, Müller LO, Toro EF. Hyperbolic reformulation of a 1D viscoelastic blood flow model and ADER finite volume schemes. *Journal of Computational Physics* 2014; :101–123.

67. Reymond P, Merenda F, Perren F, Rüfenacht D, Stergiopulos N. Validation of a one-dimensional model of the systemic arterial tree. *Am. J. Physiol. Heart Circ. Physiol.* 2009; **297**:H208–H222.
68. Chen P, Quarteroni A, Rozza G. Simulation-based uncertainty quantification of human arterial network hemodynamics. *Int. J. Numer. Meth. Biomed. Engng.* 2013; **29**:698–721.

## 7. TABLES

Case	Scheme	$\Delta t$ (ms)	$\Omega_e$ (cm)	$CFL$	Accuracy	
					Space (order)	Time (order)
Single pulse	DCG	0.1	2.00	0.18	5 <sup>th</sup>	2 <sup>nd</sup>
	LCG	0.01	0.20	0.03	2 <sup>nd</sup>	2 <sup>nd</sup>
	FEM	0.0001	0.25	NA	2 <sup>nd</sup>	1 <sup>st</sup>
	FVM	1.457	1.00	0.9	4 <sup>th</sup>	4 <sup>th</sup>
	McC	0.25	0.156	0.99	2 <sup>nd</sup>	2 <sup>nd</sup>
	STM	0.1	0.10	NA	1 <sup>st</sup>	2 <sup>nd</sup>
Carotid	DCG	1.0	12.60	0.48	5 <sup>th</sup>	2 <sup>nd</sup>
	LCG	0.2	0.17	0.8	2 <sup>nd</sup>	2 <sup>nd</sup>
	FEM	0.1	1.26	NA	2 <sup>nd</sup>	1 <sup>st</sup>
	FVM	3.27	2.00	0.9	2 <sup>nd</sup>	2 <sup>nd</sup>
	McC	0.5	0.39	0.87	2 <sup>nd</sup>	2 <sup>nd</sup>
	STM	1.0	1.00	NA	1 <sup>st</sup>	2 <sup>nd</sup>
Aorta	DCG	0.5	12.07	0.19	5 <sup>th</sup>	2 <sup>nd</sup>
	LCG	0.8	0.48	0.85	2 <sup>nd</sup>	2 <sup>nd</sup>
	FEM	0.1	1.20	NA	2 <sup>nd</sup>	1 <sup>st</sup>
	FVM	3.31	2.00	0.9	2 <sup>nd</sup>	2 <sup>nd</sup>
	McC	0.5	0.71	0.35	2 <sup>nd</sup>	2 <sup>nd</sup>
	STM	1.0	1.00	NA	1 <sup>st</sup>	2 <sup>nd</sup>
Aortic bifurcation	DCG	1.0	0.085	0.32	3 <sup>rd</sup>	2 <sup>nd</sup>
	LCG	0.2	0.17	0.85	2 <sup>nd</sup>	2 <sup>nd</sup>
	FEM	1.0	0.86	NA	2 <sup>nd</sup>	1 <sup>st</sup>
	FVM	1.99	2.00	0.9	2 <sup>nd</sup>	2 <sup>nd</sup>
	McC	0.5	0.71	0.5	2 <sup>nd</sup>	2 <sup>nd</sup>
	STM	1.0	1.00	NA	1 <sup>st</sup>	2 <sup>nd</sup>
37-Artery	DCG	0.1	2.00	0.42	3 <sup>rd</sup>	2 <sup>nd</sup>
	LCG	0.1	0.175	0.85	2 <sup>nd</sup>	2 <sup>nd</sup>
	FEM	0.1	1.00	NA	2 <sup>nd</sup>	1 <sup>st</sup>
	FVM	0.76	2.00	0.9	3 <sup>rd</sup>	3 <sup>rd</sup>
	McC	0.25	0.18	0.7	2 <sup>nd</sup>	2 <sup>nd</sup>
	STM	1.0	0.20	NA	1 <sup>st</sup>	2 <sup>nd</sup>
ADAN56	DCG	0.1	2.00	0.31	3 <sup>rd</sup>	2 <sup>nd</sup>
	LCG	0.01	0.065	0.1	2 <sup>nd</sup>	2 <sup>nd</sup>
	FEM	1.0	0.50	NA	2 <sup>nd</sup>	1 <sup>st</sup>
	FVM	0.59	1.00	0.9	3 <sup>rd</sup>	3 <sup>rd</sup>
	McC	0.5	0.45	0.8	2 <sup>nd</sup>	2 <sup>nd</sup>
	STM	0.5	0.50	NA	1 <sup>st</sup>	2 <sup>nd</sup>

Table I. Numerical parameters for all six numerical schemes in the test cases considered in this study: discontinuous Galerkin (DCG), locally conservative Galerkin (LCG), Galerkin least-squares finite element method (FEM), finite volume method (FVM), finite difference MacCormack (McC), and simplified trapezium rule method (STM). The time step is  $\Delta t$ , the characteristic spatial discretization is  $\Omega_e$ , and  $CFL = \lambda \Delta t / \Omega_e$  is the Courant-Friedrichs-Lewy number used for each scheme, where  $\lambda = \max|U + c|$ , is the maximum eigenvalue absolute value over the entire spatial domain at a given time. Space accuracy is the theoretical order of accuracy in space. NA: not applicable.

Property	Value
Length, $L$	10 m
Cross-sectional area, $A_0$	$\pi \text{ cm}^2$
Initial cross-sectional area, $A(x, 0)$	$A_0$
Initial flow velocity, $U(x, 0)$	0
Initial pressure, $P(x, 0)$	0
Wall thickness, $h$	1.5 mm
Blood mass density, $\rho$	$1050 \text{ kg m}^{-3}$
Blood viscosity, $\mu$	4 mPa s or 0
Velocity profile order, $\zeta$	9
Young's modulus, $E$	400 kPa
Diastolic pressure, $P_d$	0
External pressure, $P_{\text{ext}}$	0
Outflow pressure, $P_{\text{out}}$	0

Table II. Model parameters of the single-pulse model taken from [43]. The calculated pulse wave velocity at the initial area  $A_0$  is  $c_0 = 6.17 \text{ m s}^{-1}$ .

Property	Value
Length, $L$	126 mm
Radius at diastolic pressure, $r_d$	3 mm
Area at diastolic pressure, $A_d$	$0.28274 \text{ cm}^2$
Initial cross-sectional area, $A(x, 0)$	$0.22038 \text{ cm}^2$
Initial flow velocity, $U(x, 0)$	0
Initial pressure, $P(x, 0)$	0
Wall thickness, $h$	0.3 mm
Blood density, $\rho$	$1,060 \text{ Kg m}^{-3}$
Blood viscosity, $\mu$	4 mPa s
Velocity profile order, $\zeta$	2
Young's modulus, $E$	700.0 kPa
Diastolic pressure, $P_d$	10.933 kPa
External pressure, $P_{\text{ext}}$	0
Outflow pressure, $P_{\text{out}}$	0
Windkessel resistance, $R_1$	$2.4875 \cdot 10^8 \text{ Pa s m}^{-3}$
Windkessel compliance, $C$	$1.7529 \cdot 10^{-10} \text{ m}^3 \text{ Pa}^{-1}$
Windkessel resistance, $R_2$	$1.8697 \cdot 10^9 \text{ Pa s m}^{-3}$

Table III. Model parameters of the common carotid artery taken from [33]. The resulting wave speed at mean pressure is  $c_m = 6.74 \text{ m s}^{-1}$ .

Error	DCG	LCG	FEM	FVM	McC	STM
$\mathcal{E}_P^{RMS}$	0.20	0.24	0.23	0.28	0.24	0.24
$\mathcal{E}_Q^{RMS}$	0.39	0.26	0.28	0.29	0.30	0.29
$\mathcal{E}_{\Delta r}^{RMS}$	0.96	1.00	1.00	1.07	1.01	0.98
$\mathcal{E}_{\Delta P}^{RMS}$	4.42	4.35	4.27	4.21	4.47	4.47
$\mathcal{E}_P^{MAX}$	0.34	0.52	0.50	0.66	0.52	0.53
$\mathcal{E}_Q^{MAX}$	1.23	1.02	1.12	1.07	1.20	1.13
$\mathcal{E}_{\Delta r}^{MAX}$	1.75	1.93	1.88	2.28	1.93	1.96
$\mathcal{E}_{\Delta P}^{MAX}$	16.69	16.17	15.88	15.60	16.58	16.90
$\mathcal{E}_P^{SYS}$	-0.27	-0.27	-0.26	-0.29	-0.27	-0.26
$\mathcal{E}_Q^{SYS}$	-0.55	-0.46	-0.54	-0.58	-0.62	-0.55
$\mathcal{E}_{\Delta r}^{SYS}$	-1.65	-1.63	-1.61	-1.68	-1.63	-1.63
$\mathcal{E}_{\Delta P}^{SYS}$	-15.05	-15.37	-15.16	-14.83	-15.73	-15.76
$\mathcal{E}_P^{DIAS}$	0.28	0.28	0.27	0.29	0.28	0.27
$\mathcal{E}_Q^{DIAS}$	0.25	0.22	0.26	0.24	0.23	0.27
$\mathcal{E}_{\Delta r}^{DIAS}$	0.08	0.11	0.08	0.12	0.09	0.08
$\mathcal{E}_{\Delta P}^{DIAS}$	4.99	4.76	5.03	4.91	4.45	4.85

Table IV. Relative errors with respect to the 3-D solution (in %) as defined in Section 3.8 for the six numerical schemes at the midpoint of the common carotid artery.

Property	Value
Length, $L$	24.137 cm
Radius at diastolic pressure, $r_d$	1.2 cm
Area at diastolic pressure, $A_d$	4.5239 cm <sup>2</sup>
Initial cross-sectional area, $A(x, 0)$	3.0605 cm <sup>2</sup>
Initial flow velocity, $U(x, 0)$	0
Initial pressure, $P(x, 0)$	0
Wall thickness, $h$	1.2 mm
Blood density, $\rho$	1,060 Kg m <sup>-3</sup>
Blood viscosity, $\mu$	4 mPa s
Velocity profile order, $\zeta$	9
Young's modulus, $E$	400.0 kPa
Diastolic pressure, $P_d$	9.46 kPa
External pressure, $P_{ext}$	0
Outflow pressure, $P_{out}$	0
Windkessel resistance, $R_1$	$1.1752 \cdot 10^7$ Pa s m <sup>-3</sup>
Windkessel compliance, $C$	$1.0163 \cdot 10^{-8}$ m <sup>3</sup> Pa <sup>-1</sup>
Windkessel resistance, $R_2$	$1.1167 \cdot 10^8$ Pa s m <sup>-3</sup>

Table V. Model parameters of the upper thoracic aorta taken from [33]. The resulting wave speed at mean pressure is  $c_m = 5.17$  m s<sup>-1</sup>.

Error	DCG	LCG	FEM	FVM	McC	STM
$\mathcal{E}_P^{RMS}$	1.09	1.21	1.09	1.14	1.08	1.12
$\mathcal{E}_Q^{RMS}$	2.55	2.19	2.23	2.17	2.22	2.28
$\mathcal{E}_{\Delta r}^{RMS}$	2.32	2.41	2.33	2.44	2.33	2.90
$\mathcal{E}_{\Delta P}^{RMS}$	7.70	7.23	7.23	7.14	7.23	7.52
$\mathcal{E}_P^{MAX}$	3.54	3.55	3.26	3.18	3.27	3.30
$\mathcal{E}_Q^{MAX}$	9.13	7.20	7.04	7.07	7.04	7.40
$\mathcal{E}_{\Delta r}^{MAX}$	7.80	7.67	7.32	7.20	7.09	8.04
$\mathcal{E}_{\Delta P}^{MAX}$	31.83	29.31	29.15	29.13	29.31	31.19
$\mathcal{E}_P^{SYS}$	-0.57	-0.32	-0.56	-0.71	-0.55	-0.59
$\mathcal{E}_Q^{SYS}$	-5.56	-5.36	-5.63	-5.29	-5.58	-5.56
$\mathcal{E}_{\Delta r}^{SYS}$	-2.54	-1.93	-2.50	-2.86	-2.49	-4.48
$\mathcal{E}_{\Delta P}^{SYS}$	-8.92	-8.89	-9.29	-8.53	-9.04	-9.70
$\mathcal{E}_P^{DIAS}$	0.85	1.12	0.88	0.99	0.87	0.85
$\mathcal{E}_Q^{DIAS}$	2.75	2.67	3.09	3.48	2.67	2.95
$\mathcal{E}_{\Delta r}^{DIAS}$	1.85	2.24	1.89	2.05	1.89	0.00
$\mathcal{E}_{\Delta P}^{DIAS}$	7.32	7.24	7.60	6.37	7.32	7.47

Table VI. Relative errors with respect to the 3-D solution (in %) as defined in Section 3.8 for the six numerical schemes at the midpoint of the upper thoracic aorta.

Property	Aorta	Iliac
Length, $L$	8.6 cm	8.5 cm
Radius at diastolic pressure, $r_d$	0.86 cm	0.60 cm
Area at diastolic pressure, $A_d$	2.3235 cm <sup>2</sup>	1.1310 cm <sup>2</sup>
Initial cross-sectional area, $A(x, 0)$	1.8062 cm <sup>2</sup>	0.94787 cm <sup>2</sup>
Initial flow velocity, $U(x, 0)$	0	0
Initial pressure, $P(x, 0)$	0	0
Wall thickness, $h$	1.032 mm	0.72 mm
Blood density, $\rho$	1,060 Kg m <sup>-3</sup>	
Blood viscosity, $\mu$	4 mPa s	
Velocity profile order $\zeta$	9	
Young's modulus, $E$	500.0 kPa	700.0 kPa
Diastolic pressure, $P_d$	9.46 kPa	9.46 kPa
External pressure, $P_{ext}$	0	0
Outflow pressure, $P_{out}$	—	0
Windkessel resistance, $R_1$	—	$6.8123 \cdot 10^7$ Pa s m <sup>-3</sup>
Windkessel compliance, $C$	—	$3.6664 \cdot 10^{-10}$ m <sup>3</sup> Pa <sup>-1</sup>
Windkessel resistance, $R_2$	—	$3.1013 \cdot 10^9$ Pa s m <sup>-3</sup>

Table VII. Model parameters of the aortic bifurcation taken from [33]. The resulting wave speed at mean pressure is  $c_m = 6.26$  m s<sup>-1</sup> in the abdominal aorta and  $c_m = 7.35$  m s<sup>-1</sup> in both iliac arteries.



Site	Error	DCG	LCG	FEM	FVM	McC	STM
Midpoint aorta	$\mathcal{E}_P^{RMS}$	0.37	0.39	0.37	0.40	0.38	0.38
	$\mathcal{E}_Q^{RMS}$	0.89	0.71	0.82	0.81	0.83	0.82
	$\mathcal{E}_{\Delta r}^{RMS}$	2.48	2.43	2.55	2.49	2.48	2.45
	$\mathcal{E}_P^{MAX}$	0.61	0.67	0.65	0.68	0.66	0.66
	$\mathcal{E}_Q^{MAX}$	2.51	2.24	2.53	2.44	2.56	2.52
	$\mathcal{E}_{\Delta r}^{MAX}$	4.05	3.90	4.03	4.01	3.98	3.94
	$\mathcal{E}_P^{SYS}$	-0.53	-0.54	-0.51	-0.55	-0.53	-0.51
	$\mathcal{E}_Q^{SYS}$	-2.47	-2.23	-2.52	-2.44	-2.55	-2.52
	$\mathcal{E}_{\Delta r}^{SYS}$	-3.96	-3.86	-3.99	-4.00	-3.94	-3.93
	$\mathcal{E}_P^{DIAS}$	0.50	0.51	0.47	0.53	0.49	0.48
	$\mathcal{E}_Q^{DIAS}$	1.16	1.03	1.16	1.16	1.17	1.17
	$\mathcal{E}_{\Delta r}^{DIAS}$	-1.39	-1.37	-1.49	-1.35	-1.40	-1.41
End point aorta	$\mathcal{E}_P^{RMS}$	0.42	0.43	0.41	0.44	0.42	0.42
	$\mathcal{E}_Q^{RMS}$	1.20	1.13	1.12	1.08	1.12	0.46
	$\mathcal{E}_{\Delta r}^{RMS}$	4.07	4.02	4.14	4.08	4.08	4.05
	$\mathcal{E}_P^{MAX}$	0.73	0.75	0.72	0.80	0.74	0.73
	$\mathcal{E}_Q^{MAX}$	3.55	3.54	3.53	3.28	3.53	1.48
	$\mathcal{E}_{\Delta r}^{MAX}$	6.87	6.76	6.89	6.95	6.85	6.98
	$\mathcal{E}_P^{SYS}$	-0.71	-0.70	-0.69	-0.72	-0.70	-0.69
	$\mathcal{E}_Q^{SYS}$	-3.47	-3.53	-3.52	-3.26	-3.52	-1.08
	$\mathcal{E}_{\Delta r}^{SYS}$	-6.84	-6.73	-6.87	-6.88	-6.83	-6.90
	$\mathcal{E}_P^{DIAS}$	0.54	0.55	0.53	0.57	0.54	0.53
	$\mathcal{E}_Q^{DIAS}$	1.76	1.78	1.76	1.74	1.77	0.69
	$\mathcal{E}_{\Delta r}^{DIAS}$	-1.93	-1.92	-2.02	-1.89	-1.94	-1.88
Midpoint iliac	$\mathcal{E}_P^{RMS}$	0.45	0.45	0.44	0.47	0.45	0.44
	$\mathcal{E}_Q^{RMS}$	0.92	0.66	0.65	0.68	0.67	0.66
	$\mathcal{E}_{\Delta r}^{RMS}$	4.29	4.30	4.35	4.31	4.31	4.26
	$\mathcal{E}_P^{MAX}$	0.84	0.86	0.84	0.92	0.86	0.85
	$\mathcal{E}_Q^{MAX}$	2.33	2.00	2.01	1.80	2.01	2.02
	$\mathcal{E}_{\Delta r}^{MAX}$	7.29	7.36	7.37	7.48	7.35	7.34
	$\mathcal{E}_P^{SYS}$	-0.83	-0.83	-0.81	-0.85	-0.82	-0.81
	$\mathcal{E}_Q^{SYS}$	-1.68	-1.84	-1.81	-1.58	-1.89	-1.79
	$\mathcal{E}_{\Delta r}^{SYS}$	-7.25	-7.26	-7.27	-7.31	-7.25	-7.22
	$\mathcal{E}_P^{DIAS}$	0.55	0.55	0.54	0.57	0.54	0.54
	$\mathcal{E}_Q^{DIAS}$	1.17	1.19	1.17	1.18	1.19	1.18
	$\mathcal{E}_{\Delta r}^{DIAS}$	-2.36	-2.37	-2.45	-2.35	-2.38	-2.41

Table VIII. Relative errors with respect to the 3-D solution (in %) as defined in Section 3.8 for the six numerical schemes at three points of the aortic bifurcation: midpoint of the aorta (top), end point of the aorta (middle), and midpoint of either iliac artery (bottom).

Property	Value
Blood density, $\rho$	1,050 Kg m <sup>-3</sup>
Blood viscosity, $\mu$	2.5 mPa s
Velocity profile order, $\zeta$	9
Young's modulus, $E$	1.2 MPa
Diastolic pressure, $P_d$	0
External pressure, $P_{\text{ext}}$	0
Outflow pressure, $P_{\text{out}}$	432.6 Pa

Table IX. General model parameters of the 37-artery model taken from [46].

Arterial segment	Numerical scheme	$\mathcal{E}_P^{RMS}$ (%)	$\mathcal{E}_P^{MAX}$ (%)	$\mathcal{E}_P^{SYS}$ (%)	$\mathcal{E}_P^{DIAS}$ (%)	$\mathcal{E}_Q^{RMS}$ (%)	$\mathcal{E}_Q^{MAX}$ (%)	$\mathcal{E}_Q^{SYS}$ (%)	$\mathcal{E}_Q^{DIAS}$ (%)
Aortic arch II	DCG	1.78	3.59	-1.40	-0.42	12.32	29.58	8.78	-17.95
	LCG	1.68	3.21	-1.02	-0.93	12.34	31.83	10.02	-16.93
	FEM	1.89	3.78	-1.40	-0.17	12.02	29.00	8.81	-17.08
	FVM	1.87	3.72	-1.46	-0.30	12.11	29.13	8.75	-17.93
	McC	1.94	3.97	-1.60	-0.12	12.11	29.40	8.81	-17.74
	STM	1.84	3.76	-1.39	-0.36	12.19	29.45	8.75	-17.99
Thoracic aorta II	DCG	2.36	5.29	-0.96	1.66	25.59	67.52	60.70	-39.65
	LCG	2.17	5.03	-0.79	1.13	25.36	70.75	61.59	-35.47
	FEM	2.49	5.66	-0.97	1.97	25.26	64.93	60.39	-38.29
	FVM	2.44	5.57	-1.03	1.81	25.43	65.69	61.59	-39.26
	McC	2.53	5.70	-1.13	1.98	25.62	66.22	62.24	-38.74
	STM	2.42	5.58	-0.98	1.69	25.37	65.32	61.16	-38.77
Left subclavian I	DCG	3.09	6.13	-3.92	-3.97	14.31	38.39	-2.11	-11.57
	LCG	3.12	6.06	-3.38	-4.63	13.87	34.76	-2.92	-11.33
	FEM	3.05	6.10	-3.91	-3.72	14.17	37.89	-2.53	-10.86
	FVM	3.12	6.29	-3.96	-3.93	14.24	38.12	-2.25	-11.05
	McC	3.11	6.35	-4.09	-3.69	14.31	38.25	-2.08	-10.92
	STM	3.11	6.13	-3.80	-3.97	14.45	38.96	-1.18	-10.83
R. iliac-femoral II	DCG	3.82	9.00	-2.20	-4.13	24.49	59.63	50.20	-39.72
	LCG	3.97	9.69	-2.19	-5.57	24.17	61.14	49.23	-36.92
	FEM	3.69	8.66	-2.32	-3.67	23.90	59.28	49.99	-37.18
	FVM	3.75	9.09	-2.26	-4.04	24.19	60.61	51.42	-39.06
	McC	3.65	8.95	-2.33	-3.73	24.80	61.61	52.41	-40.21
	STM	3.75	9.32	-2.37	-4.17	24.12	60.41	51.29	-38.26
Left ulnar	DCG	2.65	7.18	-0.99	-2.68	12.74	30.14	5.37	-17.48
	LCG	2.57	6.51	-1.45	-3.54	12.42	25.91	4.30	-17.93
	FEM	2.70	7.29	-1.13	-2.34	12.43	27.75	3.63	-16.14
	FVM	2.74	7.51	-1.09	-2.54	12.70	29.30	4.60	-17.15
	McC	2.75	7.42	-1.07	-2.27	12.78	29.19	4.43	-16.80
	STM	2.74	7.46	-0.81	-2.63	12.91	29.55	5.68	-17.02
R. anterior tibial	DCG	3.25	9.87	0.57	-0.13	10.49	35.07	8.37	-15.09
	LCG	3.43	12.24	0.57	-0.80	11.05	35.80	12.37	-14.59
	FEM	3.21	9.12	0.55	0.04	9.88	31.16	8.40	-13.25
	FVM	3.30	9.42	0.66	-0.14	10.22	33.57	9.79	-14.75
	McC	3.41	10.33	0.89	0.03	10.24	34.38	9.76	-14.43
	STM	3.27	9.22	0.72	-0.15	10.24	34.54	10.32	-14.07
Right ulnar	DCG	2.54	6.32	-2.18	-3.91	11.67	31.30	16.89	-3.47
	LCG	2.58	6.88	-1.92	-4.33	11.47	28.19	17.56	-7.48
	FEM	2.66	6.36	-2.55	-3.96	11.22	29.28	15.77	-4.08
	FVM	2.49	6.32	-2.20	-3.92	11.62	30.93	16.50	-4.60
	McC	2.42	6.06	-2.15	-3.66	11.63	31.09	16.58	-4.39
	STM	2.50	6.50	-2.06	-4.09	11.73	31.58	17.40	-5.34
Splenic	DCG	2.35	6.25	-0.79	-0.14	9.44	23.74	0.09	-5.97
	LCG	2.34	6.23	0.09	-0.77	9.79	22.82	3.59	-6.75
	FEM	2.28	5.95	-0.90	0.04	9.02	22.83	-1.32	-5.46
	FVM	2.33	6.12	-0.87	-0.04	9.22	23.20	-0.58	-5.95
	McC	2.22	5.57	-0.97	-0.19	9.04	23.30	-1.47	-5.21
	STM	2.36	5.96	-0.38	-0.03	9.56	24.47	1.05	-6.40

Table X. Relative pressure and flow errors with respect to *in vitro* measurements (in %) in the 37-artery network.

Property	Value
Blood density, $\rho$	1,040 Kg m <sup>-3</sup>
Blood viscosity, $\mu$	4.0 mPa s
Velocity profile order, $\zeta$	2
Young's modulus, $E$	225 kPa
Diastolic pressure, $P_d$	10 kPa
External pressure, $P_{ext}$	0
Outflow pressure, $P_{out}$	0

Table XI. General model parameters of the ADAN56 model.

N°	Artery name	Length [cm]	p. Radius [cm]	d. Radius [cm]	$R_1$ [ $\frac{\text{dyn.s}}{\text{cm}^5}$ ]	$R_2$ [ $\frac{\text{dyn.s}}{\text{cm}^5}$ ]	$C$ [ $\frac{\text{cm}^5}{\text{dyn}}$ ]
1	aortic arch I	7.441	1.595	1.295			
2	brachiocephalic trunk	4.735	0.673	0.616			
3	aortic arch II	0.960	1.295	1.257			
4	subclavian R I	1.574	0.490	0.418			
5	common carotid R	8.122	0.448	0.333			
6	vertebral R	20.445	0.134	0.134	18104	72417	3.129E-06
7a	subclavian R II	4.112	0.418	0.230			
7b	axillary R	12.000	0.230	0.208			
7c	brachial R	22.311	0.208	0.183			
8	radial R	30.089	0.138	0.138	11539	46155	4.909E-06
9	ulnar R I	2.976	0.141	0.141			
10a	common interosseous R	1.627	0.096	0.096			
10b	posterior interosseous R	23.056	0.068	0.068	47813	191252	1.185E-06
11	ulnar R II	23.926	0.141	0.141	11749	46995	4.821E-06
12	external carotid R	6.090	0.227	0.227	9391	37563	6.032E-06
13	internal carotid R	13.211	0.277	0.277	5760	23041	9.833E-06
14	common carotid L	12.132	0.448	0.333			
15	aortic arch III	0.698	1.257	1.228			
16	external carotid L	6.090	0.227	0.227	9424	37696	6.011E-06
17	internal carotid L	13.211	0.277	0.277	5779	23118	9.801E-06
18	subclavian L I	4.938	0.490	0.348			
19a	aortic arch IV	4.306	1.228	1.055			
19b	thoracic aorta I	0.990	1.055	1.036			
20	vertebral L	20.415	0.134	0.134	19243	76972	2.944E-06
21a	subclavian L II	4.112	0.348	0.230			
21b	axillary L	12.000	0.230	0.208			
21c	brachial L	22.311	0.208	0.183			
22	radial L	31.088	0.138	0.138	11332	45329	4.998E-06
23	ulnar L I	2.976	0.141	0.141			
24a	common interosseous L	1.627	0.096	0.096			
24b	posterior interosseous L	23.056	0.068	0.068	47986	191945	1.180E-06
25	ulnar L II	23.926	0.141	0.141	11976	47905	4.730E-06
26	posterior intercostal R 1	19.688	0.140	0.140	249127	996508	2.274E-07
27	thoracic aorta II	0.788	1.036	1.022			
28	posterior intercostal L 1	17.803	0.140	0.140	255583	1022333	2.216E-07
29	thoracic aorta III	1.556	1.022	0.992			
30	posterior intercostal R 2	20.156	0.155	0.155	232434	929735	2.437E-07
31	thoracic aorta IV	0.533	0.992	0.982			
32	posterior intercostal L 2	18.518	0.155	0.155	234425	937702	2.416E-07
33a	thoracic aorta V	12.156	0.982	0.754			
33b	thoracic aorta VI	0.325	0.754	0.749			

Table XII. Parameter dataset for the ADAN56 model (see Fig. 10). p.: proximal, d.: distal. Data is rounded to an adequate number of decimal digits.

N°	Artery name	Length [cm]	p. Radius [cm]	d. Radius [cm]	$R_1$ [ $\frac{\text{dyn.s}}{\text{cm}^5}$ ]	$R_2$ [ $\frac{\text{dyn.s}}{\text{cm}^5}$ ]	$C$ [ $\frac{\text{cm}^5}{\text{dyn}}$ ]
34	celiac trunk	1.682	0.335	0.321			
35	abdominal aorta I	1.399	0.749	0.732			
36	common hepatic	6.655	0.269	0.269	3349	13394	1.692E-05
37	splenic I	0.395	0.217	0.217			
38	left gastric	9.287	0.151	0.151	343394	1373574	1.650E-07
39	splenic II	6.440	0.217	0.217	4733	18933	1.197E-05
40	superior mesenteric	21.640	0.393	0.393	2182	8728	2.596E-05
41	abdominal aorta II	0.432	0.732	0.726			
42	renal L	2.184	0.271	0.271	2263	9051	2.503E-05
43	abdominal aorta III	1.198	0.726	0.711			
44	renal R	3.772	0.310	0.310	2270	9082	2.495E-05
45	abdominal aorta IV	5.409	0.711	0.643			
46	inferior mesenteric	9.024	0.208	0.208	23913	95652	2.369E-06
47	abdominal aorta V	4.222	0.643	0.590			
48	common iliac R	7.643	0.450	0.409			
49	common iliac L	7.404	0.450	0.409			
50a	external iliac R	10.221	0.338	0.319			
50b	femoral R I	3.159	0.319	0.314			
51	internal iliac R	7.251	0.282	0.282	4146	16582	1.366E-05
52	profunda femoris R	23.839	0.214	0.214	3427	13707	1.653E-05
53a	femoral R II	31.929	0.314	0.269			
53b	popliteal R I	13.203	0.269	0.237			
54	anterior tibial R	38.622	0.117	0.117	24525	98100	2.310E-06
55a	popliteal R II	0.880	0.237	0.235			
55b	tibiofibular trunk R	3.616	0.235	0.235			
55c	posterior tibial R	38.288	0.123	0.123	21156	84625	2.677E-06
56a	external iliac L	10.221	0.338	0.319			
56b	femoral L I	3.159	0.319	0.314			
57	internal iliac L	7.251	0.282	0.282	4158	16632	1.362E-05
58	profunda femoris L	23.839	0.214	0.214	3429	13715	1.652E-05
59a	femoral L II	31.929	0.314	0.269			
59b	popliteal L I	13.203	0.269	0.237			
60	anterior tibial L	38.622	0.117	0.117	24533	98131	2.309E-06
61a	popliteal L II	0.880	0.237	0.235			
61b	tibiofibular trunk L	3.616	0.235	0.235			
61c	posterior tibial L	38.288	0.123	0.123	21166	84662	2.676E-06

Table XIII. Continuation of Table XII. Parameter dataset for the ADAN56 model (see Fig. 10). p.: proximal, d.: distal. Data is rounded to an adequate number of decimal digits.

## 8. FIGURES

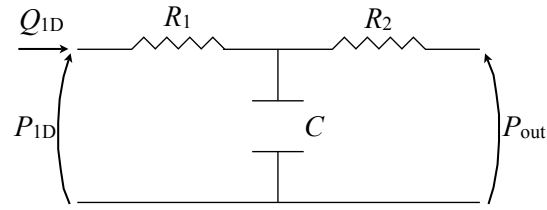


Figure 1. 1-D model terminal branches are coupled to matched three-element Windkessel models relating the outgoing flow  $Q_{1D}$  to the pressure  $P_{1D}$  at the end point of the 1-D domain. The downstream vasculature is represented by a resistance  $R_1$  connected in series with a parallel combination of a second resistance  $R_2$  and a compliance  $C$ .  $P_{out}$  is the pressure at which flow to the microcirculation ceases.



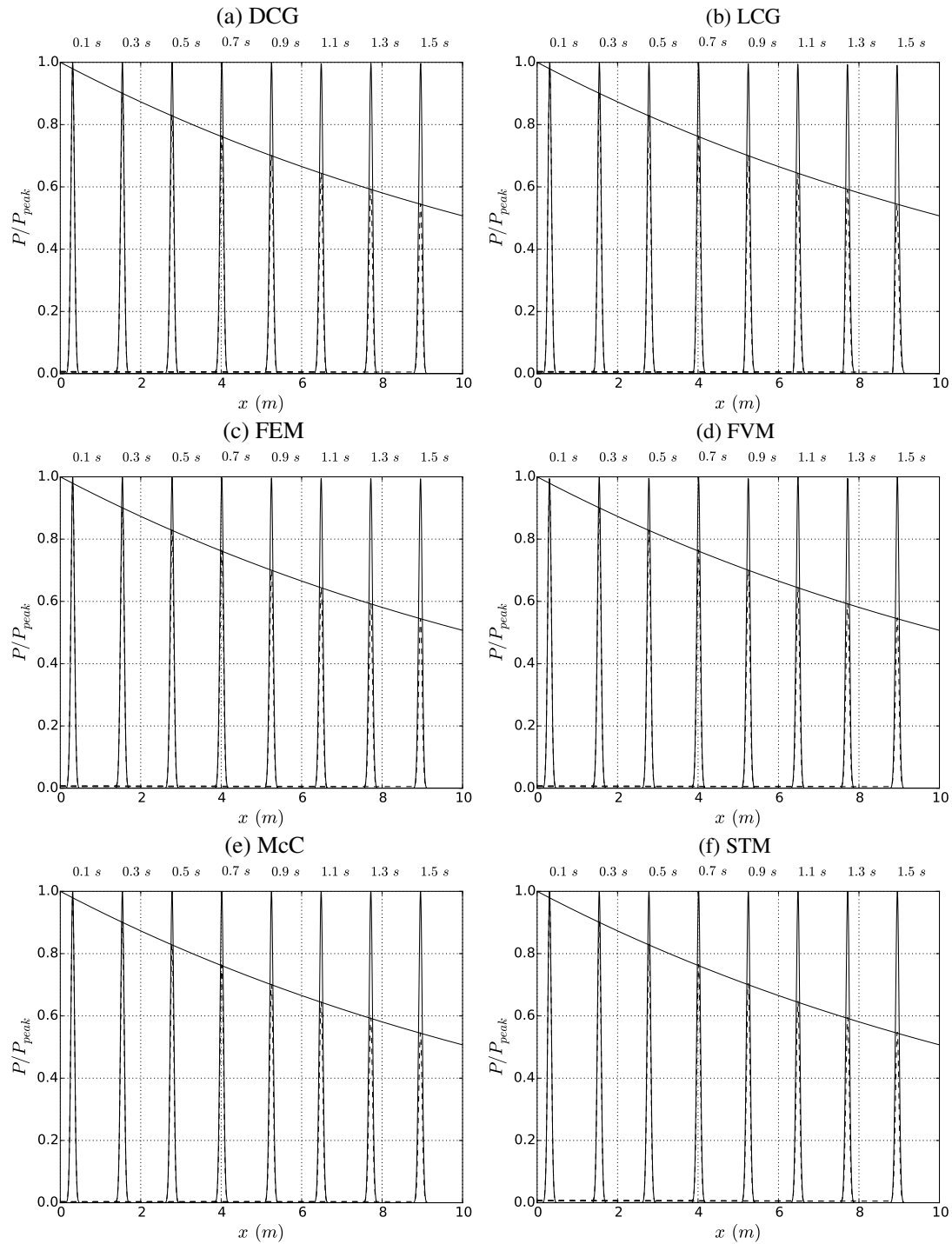


Figure 2. Single pulse. Pressure ( $P$ ) with distance for the six numerical schemes at the times indicated by the labels in a 10 m long vessel with a completely absorbent outlet. They are produced by a narrow Gaussian-shaped wave propagating from the inlet of the vessel with a peak volume inflow rate of  $1 \text{ ml s}^{-1}$ . The model parameters are shown in Table II. Two cases are shown: inviscid blood (thin solid lines) and viscous blood (dashed lines). For the viscous case, the theoretical solution of the exponential peak magnitude decay given by Eq. (15) is shown in thick black line. Pressures are normalized by the peak value of the inflow pressure ( $P_{peak}$ ).

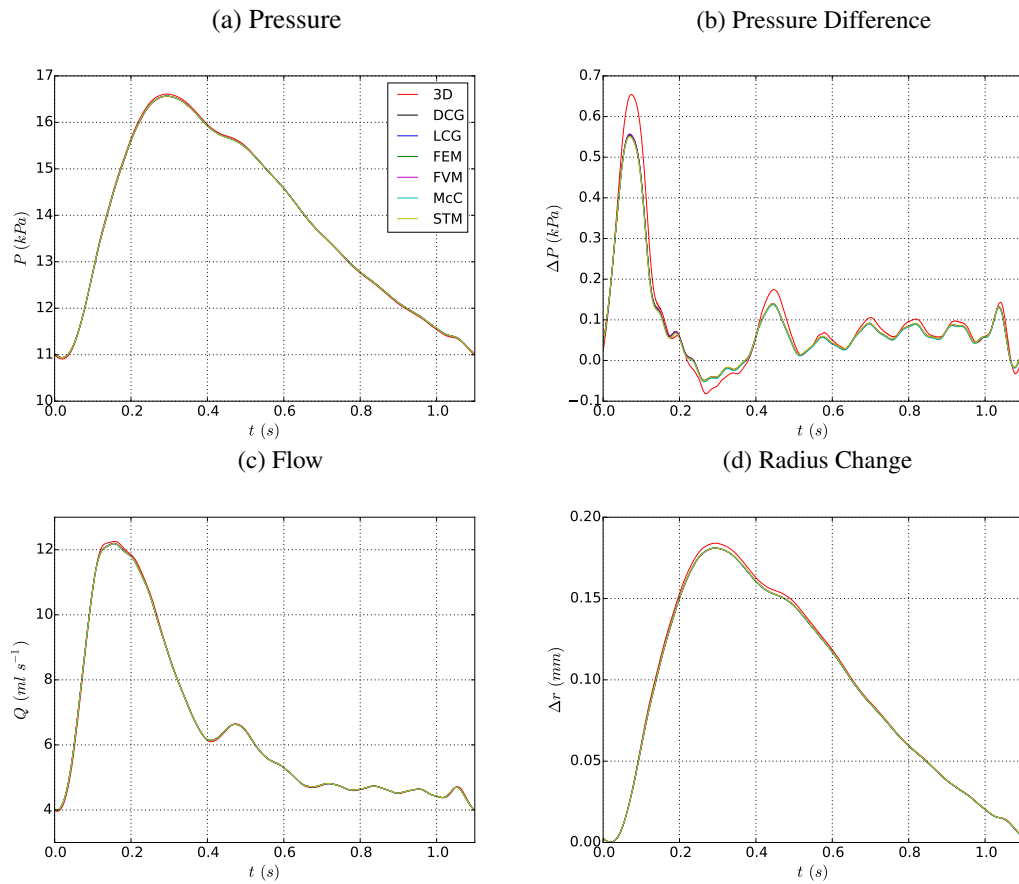


Figure 3. Common carotid artery. Pressure (a), pressure difference between inlet and outlet (b), flow rate (c), and change in radius from diastole (d) with time at the midpoint of the vessel. Results are shown for the six 1-D numerical schemes and the 3-D model from [33]. The model parameters are shown in Table III and the error calculations in Table IV.

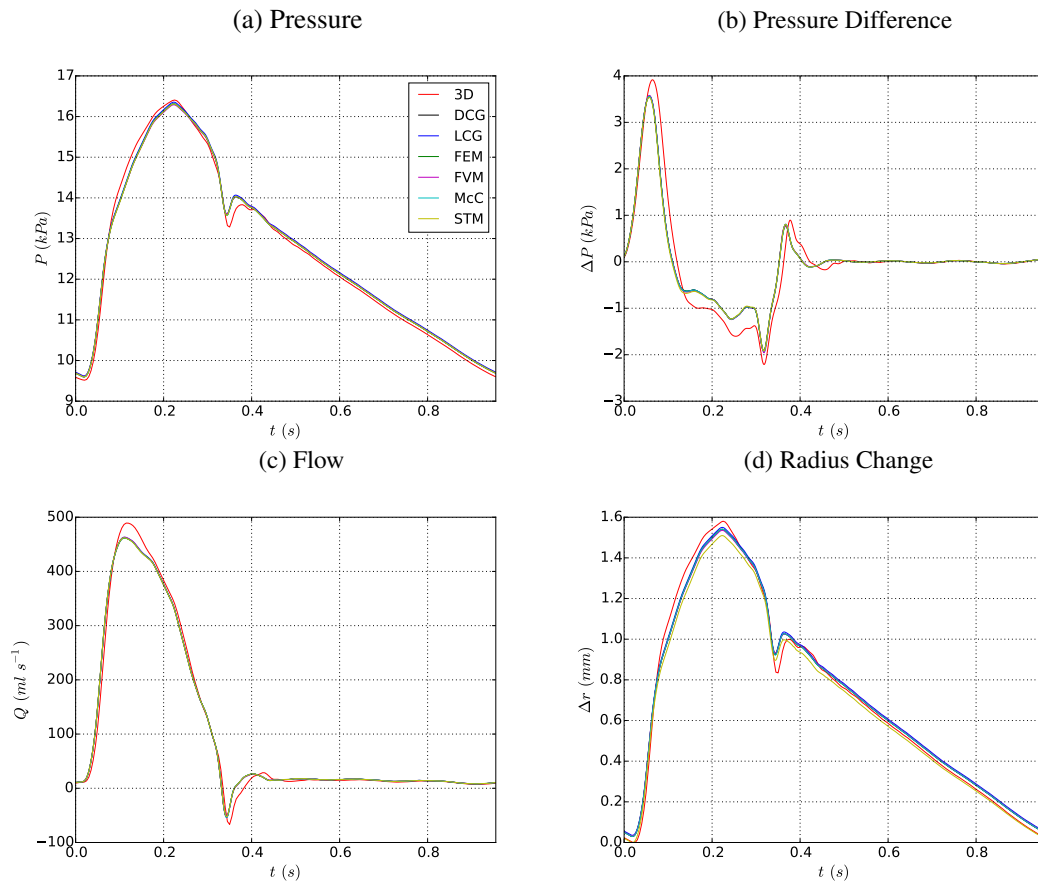


Figure 4. Upper thoracic aorta. Pressure (a), pressure difference between inlet and outlet (b), flow rate (c), and change in radius from diastole (d) with time at the midpoint of the vessel. Results are shown for the six 1-D numerical schemes and the 3-D model from [33]. The model parameters are shown in Table V and the error calculations in Table VI.

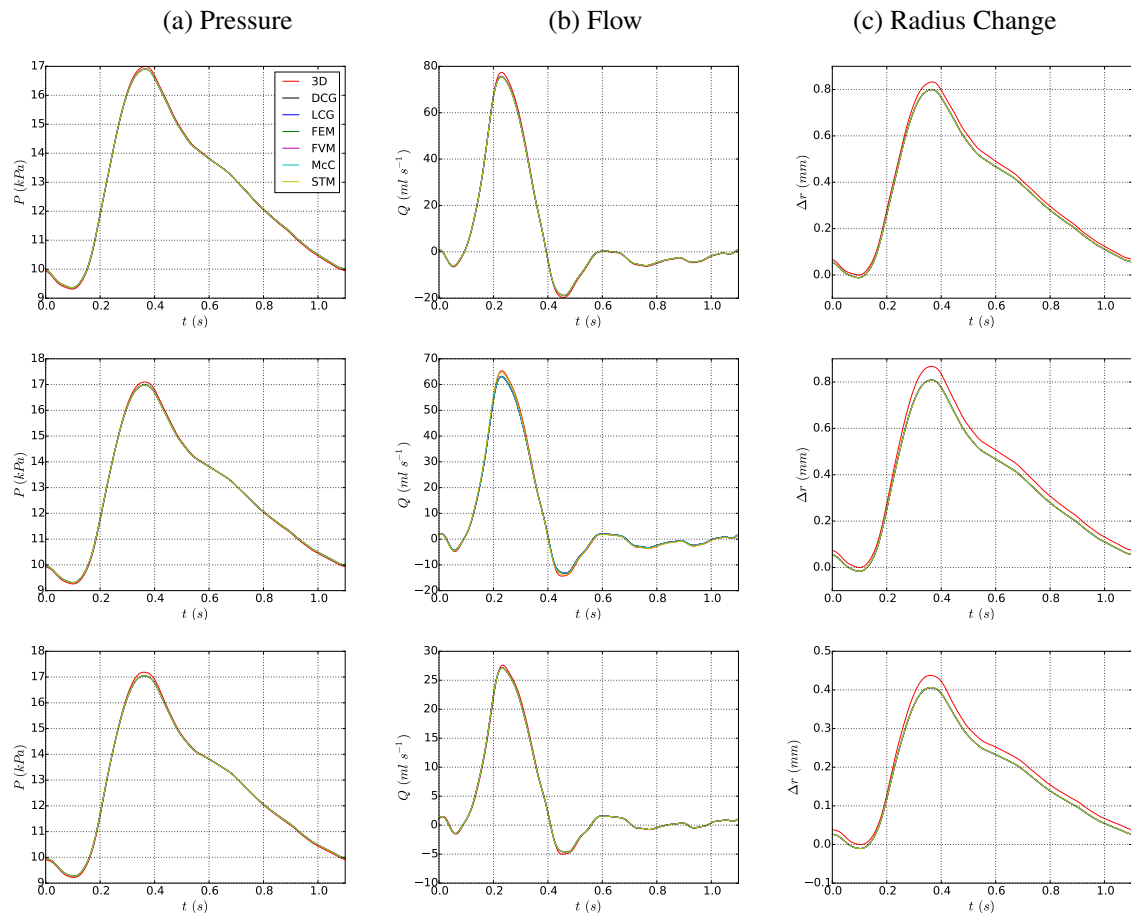


Figure 5. Aortic bifurcation. Pressure (a), flow rate (b), and change in radius from diastole (c) at the midpoint of the aorta (top), end point of the aorta (middle) and midpoint of either iliac artery (bottom). Results are shown for the six 1-D numerical schemes and the 3-D model from [33]. The model parameters are shown in Table VII and the error calculations in Table VIII.

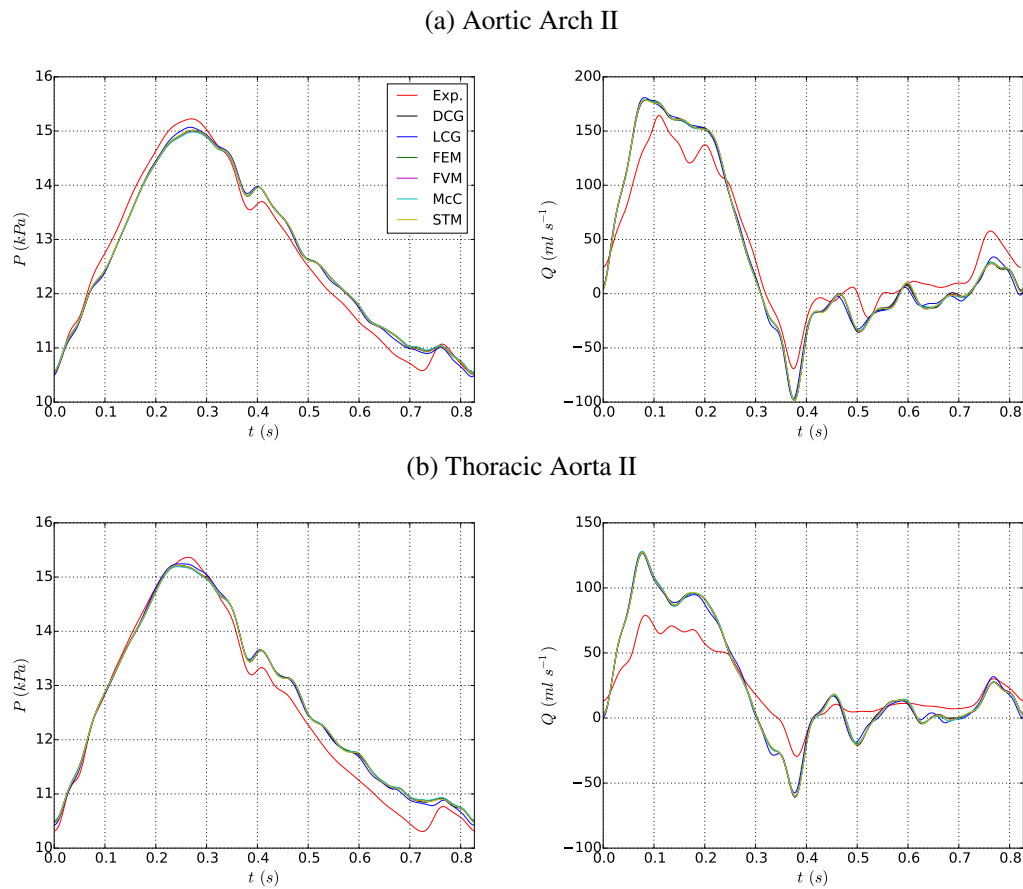


Figure 6. 37-artery network. Pressure (left) and flow (right) waveforms in the midpoint of two aortic segments: (a) aortic arch II and (b) thoracic aorta II. Results are shown for the six 1-D numerical schemes and the *in vitro* data (Exp.) measured in [46]. General model parameters are shown in Table IX.

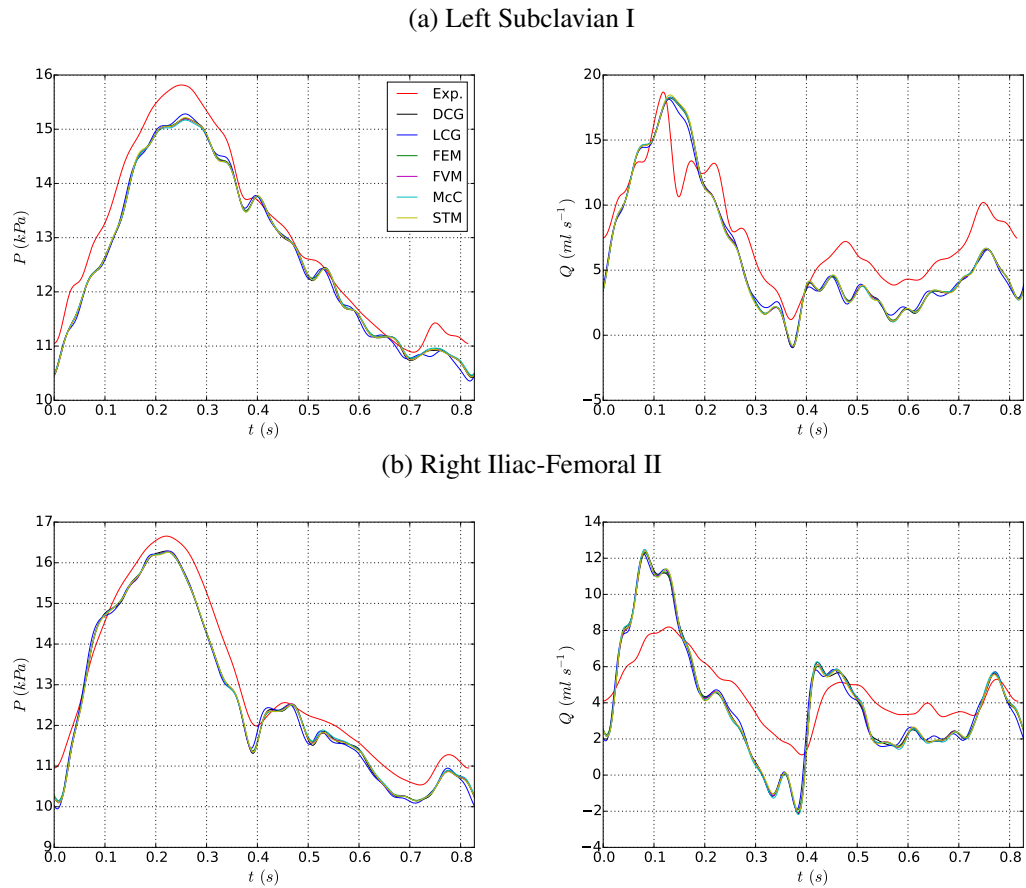
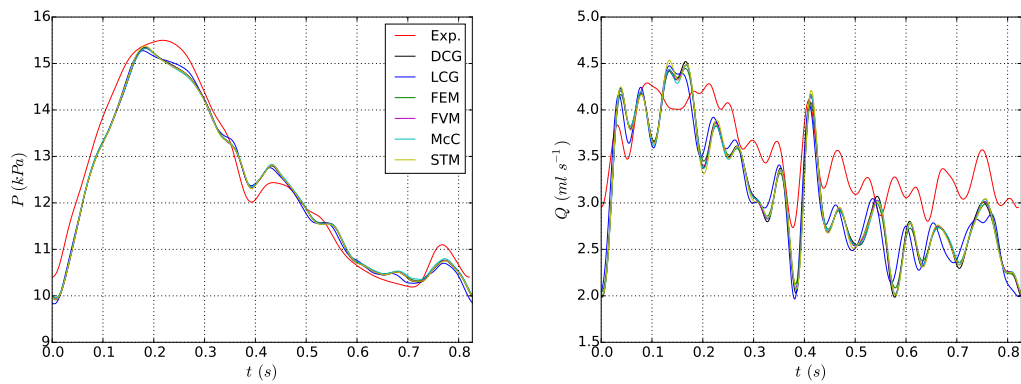


Figure 7. 37-artery network. Pressure (left) and flow (right) waveforms in the midpoint of two vessels from the first generation of bifurcations: (a) left subclavian I and (b) right iliac-femoral II. Results are shown for the six 1-D numerical schemes and the *in vitro* data (Exp.) measured in [46]. General model parameters are shown in Table IX.



(a) Left Ulnar



(b) Right Anterior Tibial

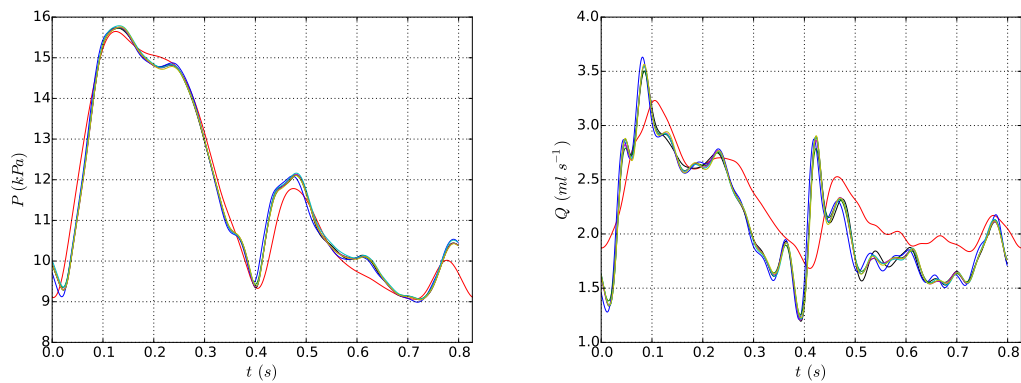


Figure 8. 37-artery network. Pressure (left) and flow (right) waveforms in the midpoint of two vessels from the second generation of bifurcations: (a) left ulnar and (b) right anterior tibial. Results are shown for the six 1-D numerical schemes and the *in vitro* data (Exp.) measured in [46]. General model parameters are shown in Table IX.

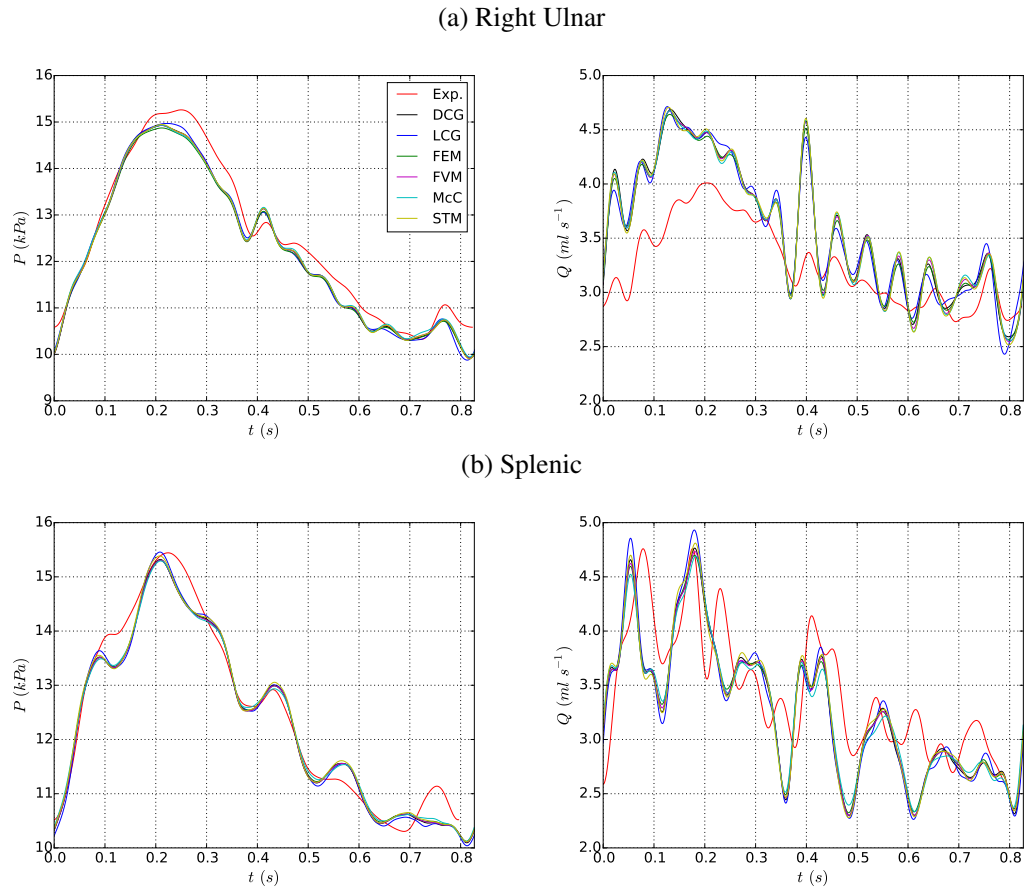


Figure 9. 37-artery network. Pressure (left) and flow (right) waveforms in the midpoint of two vessels from the third generation of bifurcations: (a) right ulnar and (b) splenic. Results are shown for the six 1-D numerical schemes and the *in vitro* data (Exp.) measured in [46]. General model parameters are shown in Table IX.

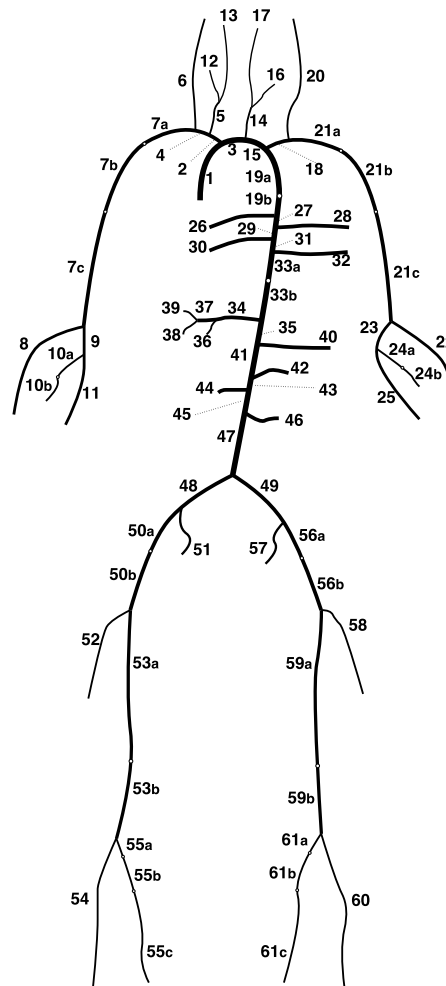
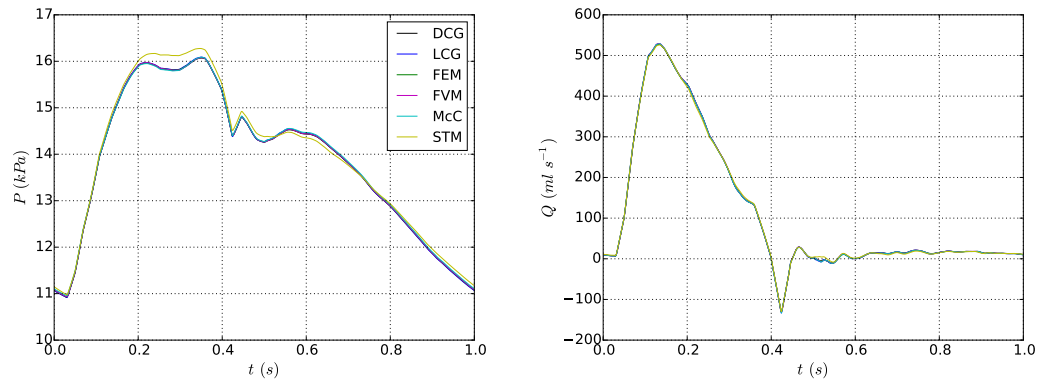
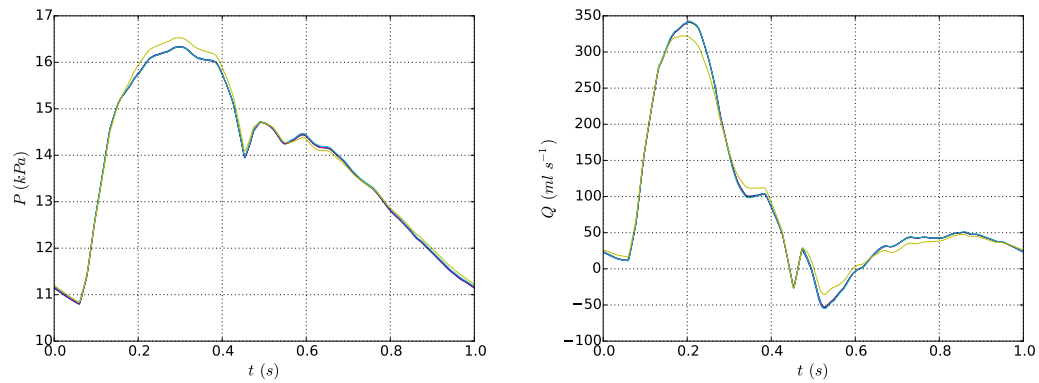


Figure 10. Topology of the ADAN56 model (see Tables XII, XIII and supplementary material).

(a) Aortic Arch



(b) Thoracic Aorta



(c) Abdominal Aorta

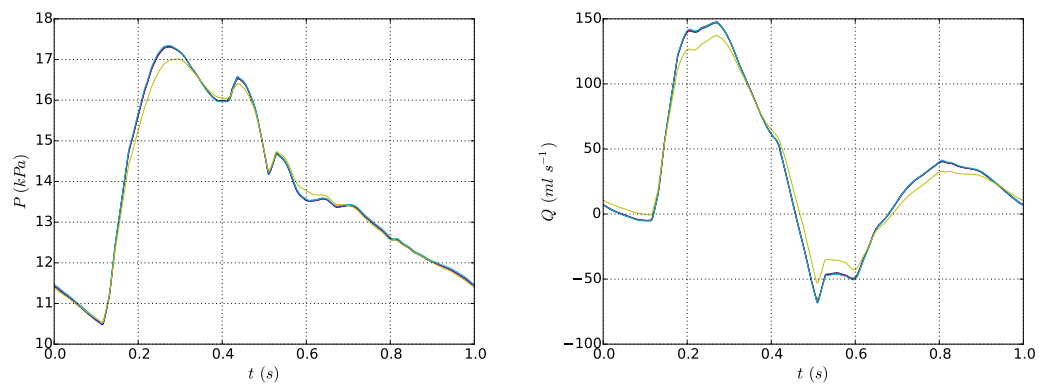
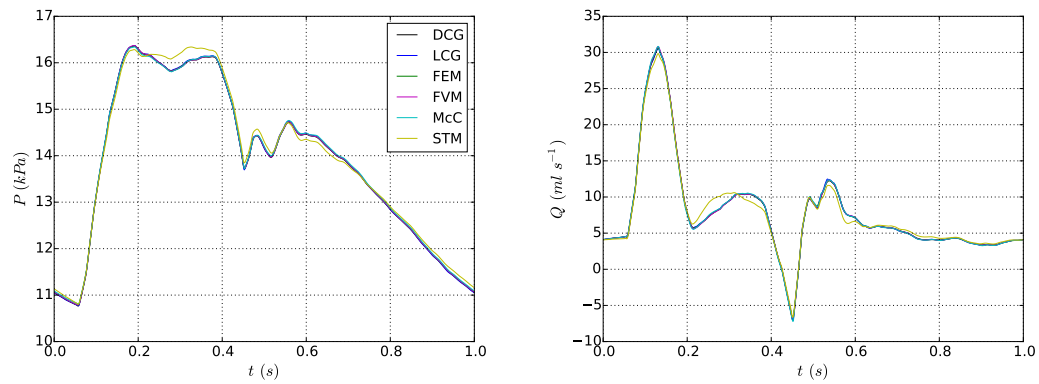
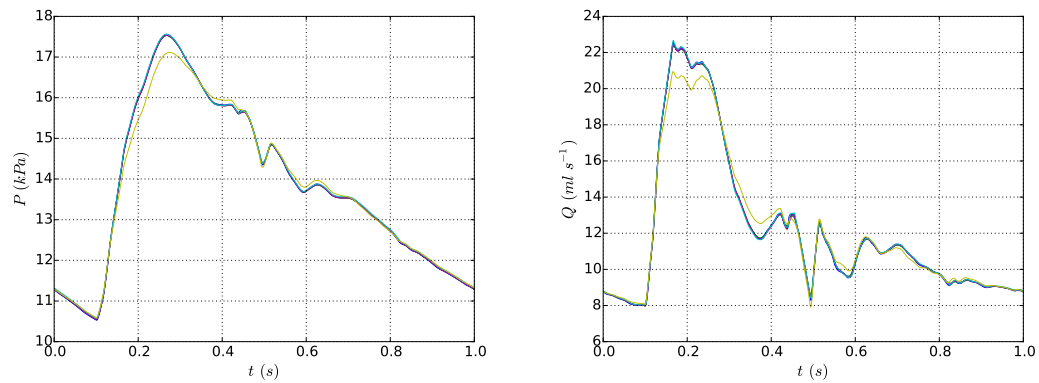


Figure 11. ADAN56 model. Pressure (left) and flow (right) waveforms in the midpoint of three aortic segments: (a) aortic arch I, (b) thoracic aorta III and (c) abdominal aorta V. Results are shown for the six 1-D numerical schemes. General model parameters are shown in Table XI.

(a) Right Common Carotid



(b) Right Renal



(c) Right Common Iliac

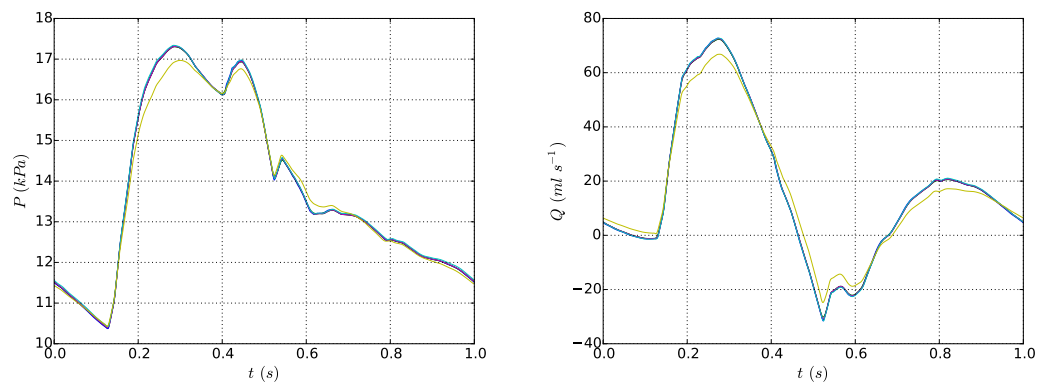
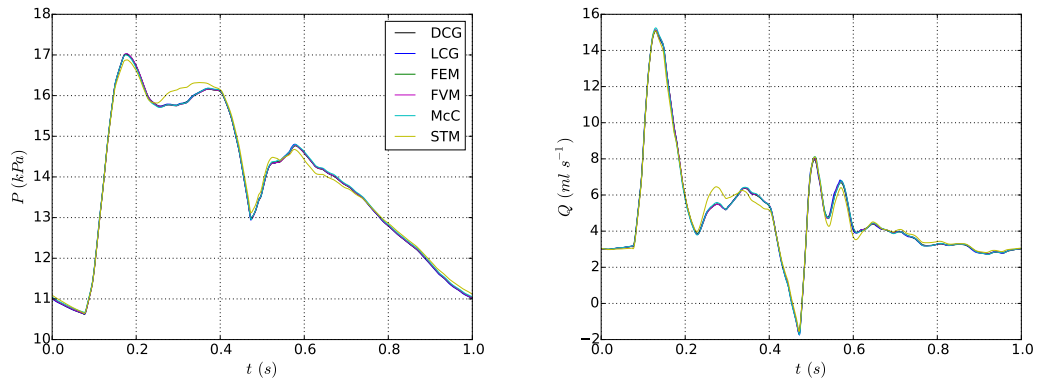
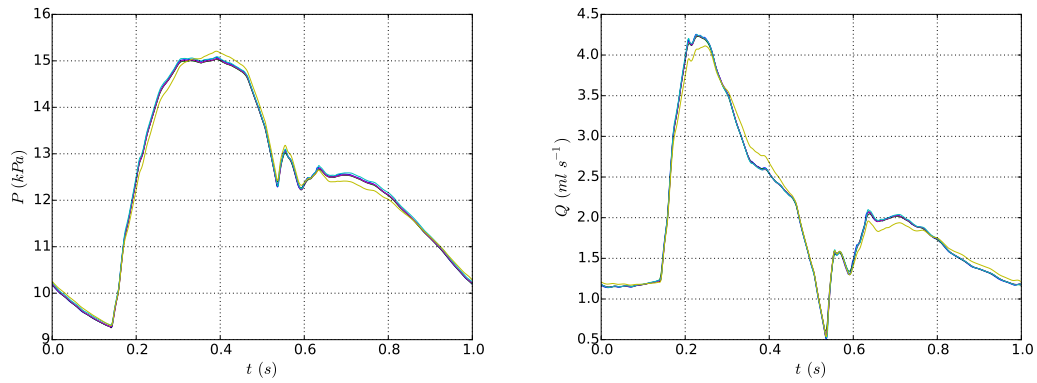


Figure 12. ADAN56 model. Pressure (left) and flow (right) waveforms in the midpoint of three vessels from the first generation of bifurcations: (a) right common carotid, (b) right renal and (c) right common iliac. Results are shown for the six 1-D numerical schemes. General model parameters are shown in Table XI.

(a) Right Internal Carotid



(b) Right Radial



(c) Right Internal Iliac

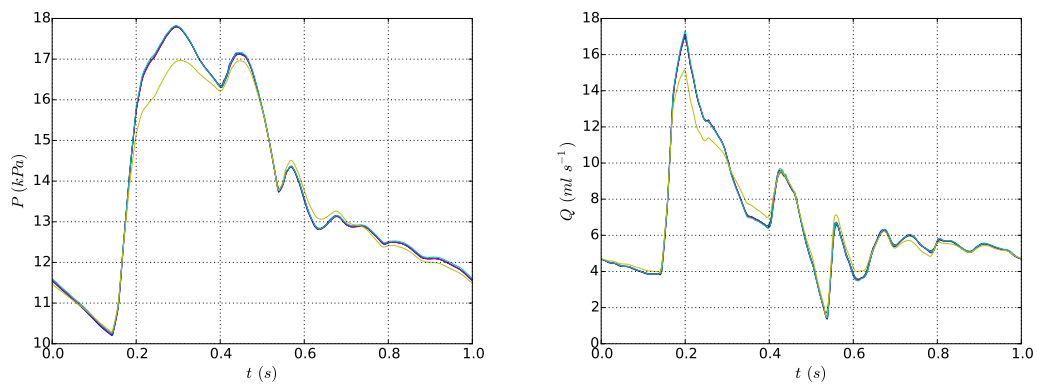


Figure 13. ADAN56 model. Pressure (left) and flow (right) waveforms in the midpoint of three vessels from the second generation of bifurcations: (a) right internal carotid, (b) right radial and (c) right internal iliac. Results are shown for the six 1-D numerical schemes. General model parameters are shown in Table XI.

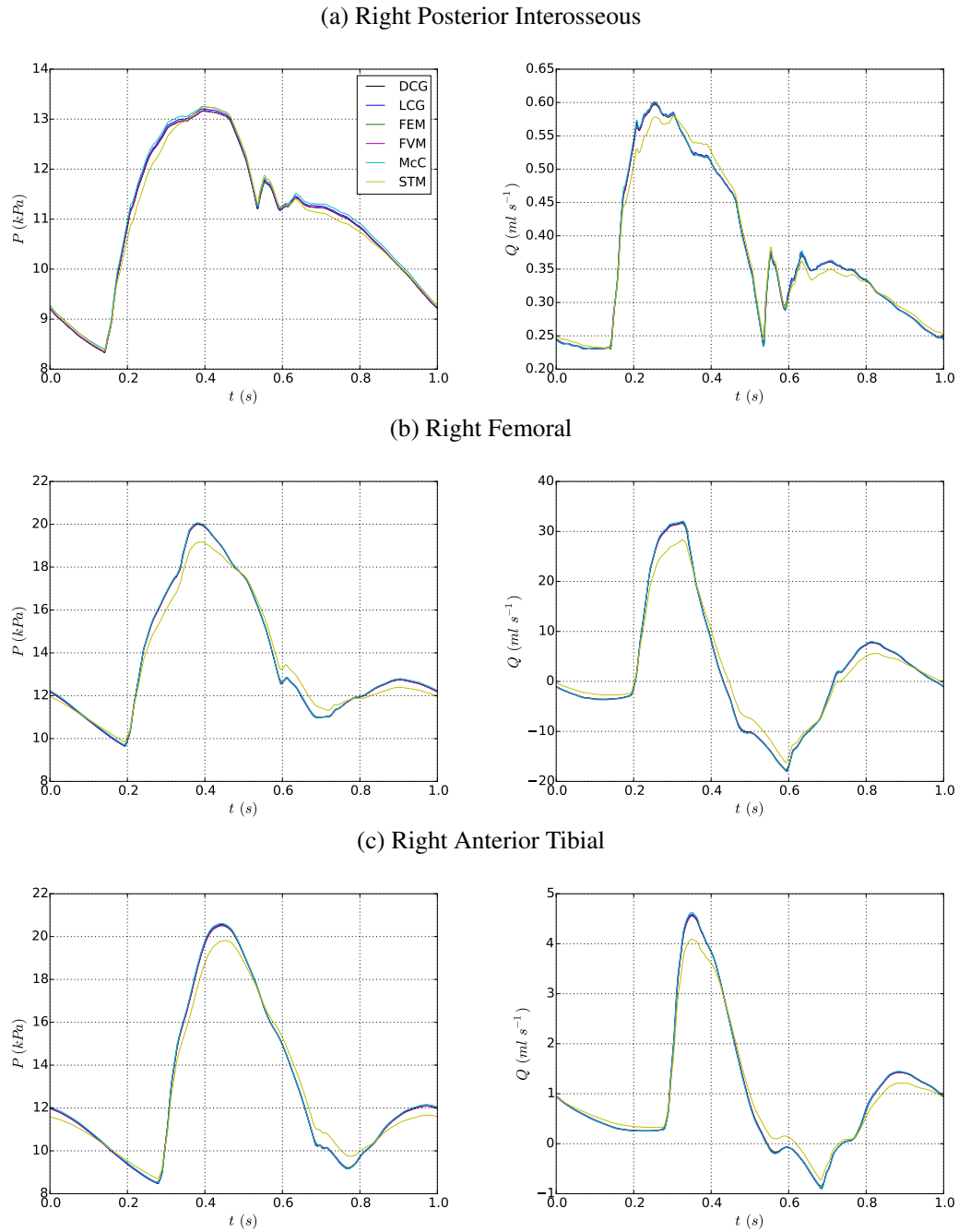


Figure 14. ADAN56 model. Pressure (left) and flow (right) waveforms in the midpoint of three vessels from the third and fourth generation of bifurcations: (a) right posterior interosseous, (b) right femoral and (c) right anterior tibial. Results are shown for the six 1-D numerical schemes. General model parameters are shown in Table XI.

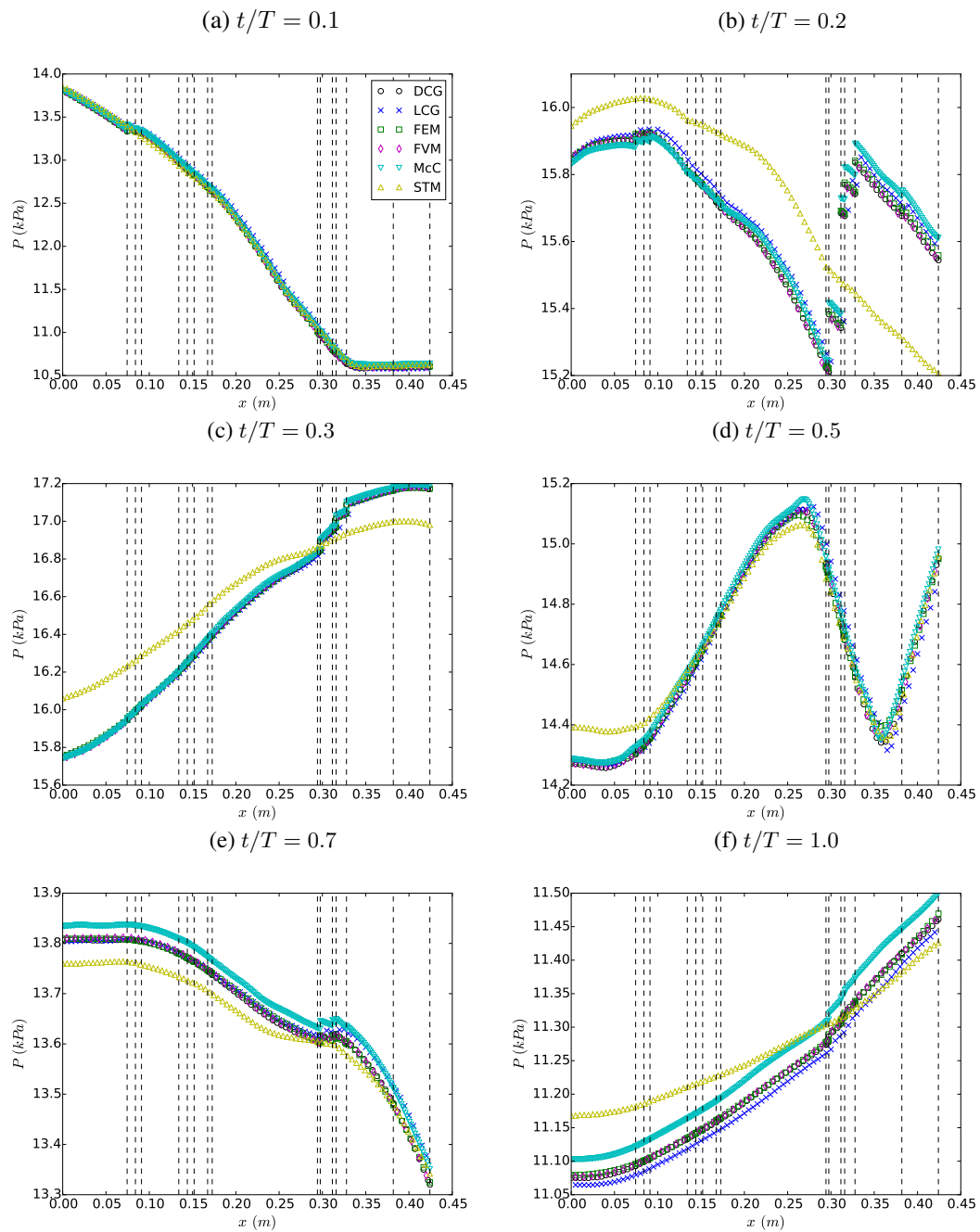


Figure 15. ADAN56 model. Pressure contour along the aorta at several time instants during the cardiac cycle, relative to the cardiac period  $T$ .



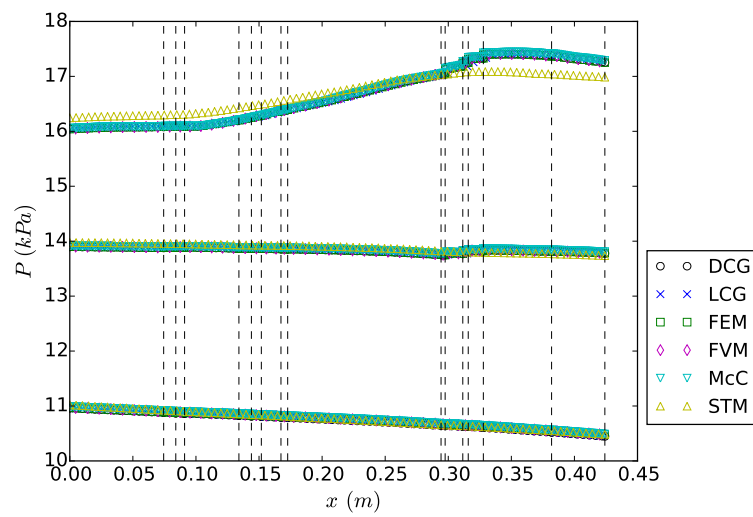


Figure 16. ADAN56 model. Systolic, mean and diastolic pressure along the aorta.